

High-Redshift Clumpy Discs & Bulges in Cosmological Simulations

Daniel Ceverino^{1*}, Avishai Dekel^{1†} and Frederic Bournaud^{2‡}

¹Racah Institute of Physics, The Hebrew University, Jerusalem 91904, Israel

²CEA, IRFU, SAp, 91191 Gif-sur-Yvette, France

ABSTRACT

We analyze the first cosmological simulations that recover the fragmentation of high-redshift galactic discs driven by cold streams. The fragmentation is recovered owing to an AMR resolution better than 70 pc with cooling below 10^4K . We study three typical star-forming galaxies in haloes of $\sim 5 \times 10^{11}M_{\odot}$ at $z \simeq 2.3$, when they were not undergoing a major merger. The steady gas supply by cold streams leads to gravitationally unstable, turbulent discs, which fragment into giant clumps and transient features on a dynamical timescale. The disc clumps are not associated with dark-matter haloes. The clumpy discs are self-regulated by gravity in a marginally unstable state. Clump migration and angular-momentum transfer on an orbital timescale help the growth of a central bulge with a mass comparable to the disc. The continuous gas input keeps the system of clumpy disc and bulge in a near *steady state* for several Gyr. The average star-formation rate, much of which occurs in the clumps, follows the gas accretion rate of $\sim 45 M_{\odot} \text{yr}^{-1}$. The simulated galaxies resemble in many ways the observed star-forming galaxies at high redshift. Their properties are consistent with the simple theoretical framework presented in Dekel, Sari & Ceverino (2009, DSC). In particular, a two-component analysis reveals that the simulated discs are indeed marginally unstable, and the time evolution confirms the robustness of the clumpy configuration in a cosmological steady state. By $z \sim 1$, the simulated systems are stabilized by a dominant stellar spheroid, demonstrating the process of “morphological quenching” of star formation (Martig et al. 2009). We demonstrate that the disc fragmentation is not a numerical artifact once the Jeans length is kept larger than ~ 7 resolution elements, i.e. beyond the standard Truelove criterion.

Key words: cosmology — galaxies: evolution — galaxies: formation — galaxies: kinematics and dynamics — galaxies: spiral — stars: formation

1 INTRODUCTION

Observations at high redshifts in the range $z \sim 1 - 3$ have opened a new window into the most active period of galaxy formation (Steidel et al. 1999; Adelberger et al. 2004; Daddi et al. 2004; Genzel et al. 2006; Förster Schreiber et al. 2006; Elmegreen et al. 2006; Genzel et al. 2008; Stark et al. 2008; Law et al. 2009; Förster Schreiber et al. 2009). Both observation and theory indicate that this was a rather violent process. Continuous, intense, cold gas streams along the cosmic web fueled dense gaseous discs and induced high star formation rates (SFR) on the order of $\sim 100 M_{\odot} \text{yr}^{-1}$ (Dekel et al. 2009), much higher than the few $M_{\odot} \text{yr}^{-1}$ in today’s galaxies. We refer to these galaxies as SFGs, standing for “Star-Forming Galaxies” and for “Stream-Fed Galaxies”. In these extreme conditions, the images of most SFGs are irregular with

giant clumps (Cowie et al. 1995; van den Bergh et al. 1996; Elmegreen et al. 2005b, 2007). Although some of these irregular morphologies may be associated with mergers or galaxy interactions, the morphology and kinematics of many of the SFGs indicates that they are rotationally supported, extended discs (Genzel et al. 2006; Förster Schreiber et al. 2006; Genzel et al. 2008). It seems that most SFGs are incompatible with being ongoing major mergers or remnants of such mergers (Shapiro et al. 2008; Bournaud et al. 2008; Dekel et al. 2009; Bournaud & Elmegreen 2009; Dekel, Sari & Ceverino 2009), though there are counter examples (e.g., Robertson & Bullock 2008). This indicates a paradigm shift in our understanding of galaxy formation.

The high-redshift galactic discs are very different from the low-redshift disc galaxies. In a typical $z \sim 2$ disc, 10 – 40% of its UV-restframe light is emitted from a few clumps of a characteristic size $\sim 1 \text{kpc}$, and with a high SFR of tens of $M_{\odot} \text{yr}^{-1}$ each (Elmegreen et al. 2004a; Elmegreen & Elmegreen 2005a; Förster Schreiber et al. 2006; Genzel et al. 2008). These clumps represent giant star-forming regions, much larger

* E-mail: ceverino@phys.huji.ac.il

† E-mail: dekel@phys.huji.ac.il

‡ E-mail: frederic.bournaud@cea.fr

than the star-forming complexes in local galaxies. This pronounced clumpy morphology at high redshift is not limited to the UV as the main high-redshift clumps are also seen in optical rest-frame emission (Genzel et al. 2008; Förster Schreiber et al. 2009). It is not a bandshift effect in the sense that the UV images of clumpy low-redshift galaxies would not appear so clumpy if put at high redshift and observed with limited resolution and signal-to-noise ratio (Elmegreen et al. 2009). The clumpy galaxies were first dubbed “clump-clusters” galaxies and “chain” galaxies when viewed face on or edge on respectively (Cowie et al. 1995; Elmegreen et al. 2004b). Most of the massive ones are thick rotating discs, with high velocity dispersions of $\sigma = 20 - 80 \text{ km s}^{-1}$ (one dimensional) and rotation to dispersion ratio of $V/\sigma \sim 1 - 7$ (Cresci et al. 2009), as opposed to today’s thin discs of $\sigma \simeq 10 \text{ km s}^{-1}$. The smaller galaxies contain a large fraction of dispersion-dominated systems (Law et al. 2007, 2009; Förster Schreiber et al. 2009). Estimates of the total gas fraction in SFGs, based on CO measurements, range from 0.2 to 0.8, with an average of $\sim 0.4 - 0.6$ (Tacconi et al. 2008; Daddi et al. 2008, 2009), systematically higher than the typical gas fraction of ~ 0.1 in today’s discs. This gas consists of large molecular cloud complexes that host the observed star-forming regions. The typical age of the stellar populations in these clumps are crudely estimated to range from one to several hundreds Myr (Elmegreen et al. 2009; Förster Schreiber et al. 2009), on the order of ten dynamical times, indicating that the clumps may plausibly survive for such durations.

A substantial fraction of these high- z clumpy discs show a central stellar bulge (Genzel et al. 2008; Elmegreen et al. 2008c). Other observations indicate that a large population of compact, massive spheroids with suppressed SFR is already present at those redshifts (Kriek et al. 2006; van Dokkum et al. 2008; Kriek et al. 2009). This means that a well-developed Red Sequence was already in place at $z \sim 2$. While major mergers do lead to spheroids (Robertson et al. 2006; Cox et al. 2006; Dekel & Cox 2006; Hopkins et al. 2006), the major-merger rate is not enough for producing spheroids in the observed abundance (Dekel et al. 2009; Genel et al. 2008; Stewart et al. 2009, and references therein), so an additional and complementary mechanism must have been working efficiently at high redshifts.

The gravitational fragmentation of gas-rich and turbulent galactic discs into giant clumps, and their subsequent migration into a central bulge, have been addressed before in the simplified context of isolated galaxies (Noguchi 1999; Elmegreen et al. 2005b; Bournaud et al. 2007; Genzel et al. 2008; Elmegreen et al. 2008a). According to the standard Toomre instability analysis (Toomre 1964), the material in a rotating disc becomes unstable to local gravitational collapse if its surface density is sufficiently high for its self-gravity to overcome the forces induced by differential rotation and velocity dispersion that work against the collapse. If the disc is maintained in a marginally unstable state with relatively high velocity dispersion, the clumps are big. Then, the timescale for their migration to the centre by gravitational interactions is short, on the order of ten disc dynamical times, or a couple of orbital periods at the disc radius.

The clumps and the other transient perturbations in the

disc drive further inflow of disc mass toward the centre through angular-momentum transport outward. Together they lead to a rapid growth of a bulge in about 0.5 Gyr, at the expense of the draining and stabilization of the disc.

The large fraction of clumpy massive galaxies at $z \sim 2$ (e.g., Elmegreen et al. 2007; Tacconi et al. 2008) suggests that the clumpy phase should last for a few Gigayears. DSC have argued that when a galaxy is part of the high-redshift cosmological environment, it can naturally be in a long-term steady state typically consisting of a clumpy disc and a comparable bulge. Massive galaxies at that epoch are fed by continuous, intense cold gas streams that follow the filaments of the cosmic web (Kereš et al. 2005; Dekel & Birboim 2006; Ocvirk et al. 2008; Dekel et al. 2009). The fresh supply of cold gas refills the disc as it is being drained into the bulge, and keeps the surface density sufficiently high for disc instability and new clump formation as long as the bulge is not too massive. On the other hand, if a large fraction of the incoming streams is already in clumps, they can stabilize the disc against fragmentation in two complementary ways: by rapid direct buildup of the bulge via mergers and by generating high velocity dispersion in the disc. This led DSC to suggest that a low level of clumpiness in the streams is a key factor in maintaining a clumpy disc in steady state.

This long-term clumpy phase can be naturally addressed by cosmological, hydrodynamical simulations, though the numerical challenges are not trivial. The dynamical range must explore the cosmological streams on scales of hundreds of kpc while properly resolving the gas physics in the disc on scales of tens of parsecs. These difficulties limited the earlier simulations of disc fragmentation to idealized discs in isolation (Noguchi 1999; Immeli et al. 2004a,b; Bournaud et al. 2007; Elmegreen et al. 2008a; Bournaud & Elmegreen 2009; Bournaud et al. 2009). They successfully reproduced the Toomre instability, the subsequent migration of clumps and the formation of a classical bulge. However, in the absence of fresh cosmological gas supply, these phenomena were limited to one episode of instability and disc evacuation, and were not capable of capturing the long-term cosmological steady state. On the other hand, the earlier simulations that did follow the cosmological gas supply did not have the necessary resolution with proper gas physics to reproduce the gravitational fragmentation of the discs (Springel & Hernquist 2003; Kereš et al. 2005; Governato et al. 2007; Ocvirk et al. 2008; Dekel et al. 2009).

A key ingredient for recovering the fragmentation is allowing the gas to cool to temperatures below 10^4 K and reach densities well above 1 atom per cc, typical of gas in giant molecular clouds. If the gas is kept at higher temperatures, the pressure prevents local gravitational collapse. This may be fine in the modeling of present-day disks that do not suffer from wild gravitational instability (Springel & Hernquist 2003; Robertson et al. 2004), but it is not adequate when simulating the high-redshift gaseous and continuously fed disks that are likely to develop wild disk instabilities.

Even with state-of-the-art resolution of ~ 30 pc, where the gas can cool to ~ 100 K and reach $n \sim 100 \text{ cm}^{-3}$ (Ceverino & Klypin 2009; Agertz et al. 2009b), the thermal

Jeans scale in the dense gas is below the resolution scale. In other words, there is no pressure to support the gas against gravitational collapse on the resolution scale, so the gas tends to fragment artificially (Truelove et al. 1997; Bate & Burkert 1997). In order to prevent artificial fragmentation, the common procedure is to introduce a pressure floor (Machacek et al. 2001; Robertson & Kravtsov 2008; Agertz et al. 2009a), but it has to be applied in a way that would not prevent real fragmentation on the turbulence Jeans scale when it is only a few times the resolution scale.

In this paper we present the results from three different high-resolution cosmological simulations, zooming in on three nearby random galaxies with haloes of $\sim (1 - 2) \times 10^{12} M_\odot$ at $z = 1$. They have reached $\sim 5 \times 10^{11} M_\odot$ at $z = 2.3$, where we perform a detailed analysis. In these simulations, we do allow cooling to temperatures well below 10^4K and thus allow for real physical disc fragmentation, while applying the pressure floor necessary for preventing artificial fragmentation. We find that they all show clumpy discs similar to the observations and according to theory. In §2 we summarize the theoretical framework laid out in DSC. In §3 we describe the simulation method. In §4 we address the global properties of the simulated galaxies and verify that they obey the observed scaling relations at high redshift. In §5 we study in detail the three simulated galaxies at $z = 2.3$ where we focus on the disc fragmentation and bulge formation, in comparison with theory and observations. §5.2 brings projected images of the different galaxy components, §5.3 compares simulated and observed images, §5.4 describes the properties of the clumpy discs and bulges in comparison to the theory as laid out in DSC, §5.5 refers to a two-component instability analysis, §5.6 follows the formation of disc clumps and their migration to the bulge, and §5.7 highlights the cosmological steady state of clumpy discs, and the possible eventual stabilization by a massive spheroid. In §6 we test the robustness of our results to artificial fragmentation. Finally, in §7 we summarize our results and discuss them.

2 THEORETICAL FRAMEWORK

In a companion paper, DSC have laid out a simple theoretical framework for clumpy discs driven by cosmological cold streams at high-redshift. We summarize the theory here to help us interpret the simulation results as we present them. Note that the theoretical expectations did not affect the numerical experiments themselves in any way.

Well before $z \sim 1$, the high accretion rate is expected to keep the discs gas rich, which validates a simplified one-component analysis as a first crude approximation. According to the standard Toomre instability analysis (Toomre 1964; Binney & Tremaine 2008, Chapter 6) a rotating disc becomes unstable to axi-symmetric modes once the local gravity overcomes both differential rotation and pressure due to turbulence or thermal motions. This is expressed in terms of the local stability parameter Q being smaller than a critical value of order unity,

$$Q = \frac{\sigma_r \kappa}{\pi G \Sigma} < Q_c. \quad (1)$$

Here Σ is the surface density of the disc at radius r , σ_r

is the radial velocity dispersion, (or the gas sound speed if it is larger), and κ is the epicyclic frequency. We adopt $\kappa = \sqrt{3}\Omega$, where Ω is the angular circular velocity. The factor $\sqrt{3}$ stands for a number between 1 and 2, depending on the shape of $\Omega(r)$. For a thick disc, $Q_c \simeq 0.68$ (Goldreich & Lynden-Bell 1965).

The disc of mass M_d is expected to develop transient elongated sheared features and to fragment into a few bound massive clumps of a typical mass

$$M_c \simeq 0.27 \delta^2 M_d \quad (2)$$

and a typical radius

$$R_c \sim 0.52 \delta R_d, \quad (3)$$

where δ is the disc fraction of the total mass within the disc radius R_d ,

$$\delta \equiv \frac{M_d}{M_{\text{tot}}(R_d)}. \quad (4)$$

The fraction of disc mass in the clumps is crudely estimated to be in the range $\alpha \sim 0.1 - 0.4$. Note that a higher δ corresponds to more massive clumps.

An unstable disc is expected to self-regulate itself at $Q \simeq Q_c$ with a velocity dispersion-to-rotation ratio

$$\frac{\sigma_r}{V} \simeq 3^{-1/2} Q_c \delta. \quad (5)$$

The turbulence can be largely maintained by the gravitational encounters of the clumps themselves, which operate on a timescale $t_{\text{enc}} \simeq 2.1 Q^2 \alpha^{-1} t_d$, where $t_d \equiv \Omega^{-1} \simeq 50 \text{Myr}$ is the disc dynamical time. With $Q \simeq 0.67$ and $\alpha \simeq 0.2$, this matches the timescale for turbulence decay, $t_{\text{dis}} \simeq 1.4 Q^{-1} t_d$. The estimated effect of clump encounters is a lower limit to the total effect of the gravitational interactions involving all the components of the perturbed disc, which maintain the marginally unstable configuration. A higher δ thus corresponds to a higher σ_r/V and a thicker disc.

The same gravitational encounters and dynamical friction make the giant clumps migrate to the centre on a timescale

$$t_{\text{mig}} \simeq 2.1 Q^2 \delta^{-2} t_d \quad (6)$$

and grow a bulge. The associated evacuation timescale for the entire disc mass is $t_{\text{evac}} \simeq 10.5 \alpha_{.2}^{-1} Q^2 \delta^{-2} t_d$. Additional comparable contributions to mass inflow in the disc are associated with angular-momentum transport outward, partly induced by the clump migration and partly due to torques involving the transient features. We noted that a higher δ corresponds to more massive clumps. Then, With $Q \sim Q_c$, a higher δ or σ_r/V , namely more massive clumps, correspond to a more rapid migration.

At high redshift, the continuous gas supply can maintain the disc unstable with giant clumps for several Gigayears. The average cosmological gas accretion rate (Neistein et al. 2006; Genel et al. 2008) is expected to be

$$\dot{M} = 6 M_{12}^{1.15} (1+z)^{2.25} f_{0.16} M_\odot \text{yr}^{-1} \quad (7)$$

where M_{12} is the halo virial mass in units of $10^{12} M_\odot$, and $f_{0.16}$ is the baryon fraction in units of 0.16. Based on the the effective deep penetration seen in cosmological simulations (Dekel et al. 2009), the cosmological streams feed baryons

into massive galaxies on a timescale $t_{\text{acc}} \simeq 44\tau^{-1}t_{\text{d}}$, with $\tau \simeq 1$ at $z = 2$ and varying from 2.5 to 0.4 between $z \simeq 9$ and 1. The smooth component of the incoming streams, including small clumps, replenishes the evacuating disc, while the massive clumps associated with the incoming streams merge to the bulge. If the galaxy streams in which the massive clump fraction is less than average, the system is predicted to settle into a near steady state with $\delta \simeq 0.3$, i.e., the input by streams and the transport from disc to bulge maintain a constant bulge-to-disc ratio near unity. This corresponds to comparable contributions of disc, bulge and dark matter to $M_{\text{tot}}(R_{\text{d}})$.

On the other hand, in galaxies where the incoming streams are more clumpy than average, the merging of external massive clumps (possibly associated with dark matter haloes) are expected to grow a dominant spheroid with $\delta < 0.25$, and the dense clumps are capable of stirring up the turbulence in the disc to levels that stabilize the disc. DSC thus hypothesized that the dependence of the instability on the degree of clumpiness in the streams introduces a robust bimodality in the galaxy properties starting at $z \gtrsim 3$.

If the properties of the streams feeding a given galaxy vary in time, and in particular if the degree of clumpiness in these streams evolves, the galaxy may go through transitions from an unstable disc-dominated configuration to a stable bulge-dominated state and vice versa (Martig et al. 2009). The instability can be responsible for efficient star formation while the stability may result in a significant suppression of star formation. However, after $z \sim 2$, the recovery from a bulge-dominated system back to an unstable disc takes several Gigayear and may never materialize.

A systematic change in the stream properties is expected after $z \sim 1 - 2$. Then, the cosmological accretion rate becomes slower, the smooth cold streams no longer penetrate very effectively through the shock-heated media in massive haloes of $\sim 10^{12}M_{\odot}$ or higher (Kereš et al. 2005; Dekel & Birnboim 2006; Cattaneo et al. 2006; Ocvirk et al. 2008), and the input becomes dominated by stars rather than gas. Once the accretion cannot replenish the gas discs on a time scale comparable to the timescale for the discs to turn into clumps and stars, the galaxies gradually become dominated by old stars and eventually stable against axi-symmetric modes. This is because, unlike the dissipating turbulent gas, the stars maintain the velocity dispersion that they have acquired during their history. While the young stars are expected to have a velocity dispersion comparable to that of the gas and therefore to follow the gas into the bound clumps, the older stars are likely to have a higher σ . They therefore tend to form transient perturbations rather than accumulate in bound clumps, and eventually they join the stable component that just adds to the potential well and thus helps stabilizing the whole system.

The axi-symmetric instability of a two-component disc has been studied by Jog & Solomon (1984) and Rafikov (2001). Denoting the velocity dispersions of stars and gas σ_{s} and σ_{g} respectively (with the latter standing for the speed of sound if thermal pressure dominates), and defining Q_{s} and Q_{g} following eq. (1) separately for each component, the effective Q relevant for the instability of the combined system is approximately

Table 1. Simulations details

Comoving box size	28.57 Mpc
Number of DM particles	7×10^6
DM mass resolution	$5.5 \times 10^5 M_{\odot}$
Max. resolution (proper)	35-70 pc
Min. mass of a stellar particle	$10^4 M_{\odot}$

$$Q^{-1} = 2Q_{\text{s}}^{-1} \frac{q}{1+q^2} + 2Q_{\text{g}}^{-1} \frac{\sigma_{\text{gs}}q}{1+\sigma_{\text{gs}}^2q^2}, \quad (8)$$

where $\sigma_{\text{gs}} \equiv \sigma_{\text{g}}/\sigma_{\text{s}}$ and q is the dimensionless wave number $q \equiv k\sigma_{\text{s}}/\kappa$. The first term has to be slightly modified to take into account the dissipationless nature of the stars but this correction makes only a small difference (Rafikov 2001). The system is unstable once $Q < 1$. The most unstable wavelength corresponds to the q that minimizes Q ; it lies between $q = 1$ for $\sigma_{\text{gs}} = 1$ and $q \simeq \sigma_{\text{gs}}^{-1}$ for $\sigma_{\text{gs}} \ll 1$. Note that with $\sigma_{\text{s}} > \sigma_{\text{g}}$, the stellar disc by itself may tend to be less unstable than the gas disc by itself, $Q_{\text{s}} > Q_{\text{g}}$, but through its contribution to the self-gravity that drives the instability, the stellar disc can help the gas component de-stabilize the disc. The combined system can be unstable even when each of the components has a Q value above unity. If, for example, $\Sigma_{\text{g}} = \Sigma_{\text{s}}$ and $\sigma_{\text{gs}} = 0.5$, the error made in Q_{c} by ignoring the higher velocity dispersion of the stars is about 30%. If, on the other hand, $\sigma_{\text{gs}} \ll 1$, the gas disc has to be treated on its own while the stars become part of the stabilizing component.

The typical low-redshift discs are thus very different from the clumpy high-redshift discs. In a bulge-dominated, cold disc, supernova and stellar feedback may have an additional effect on the stabilization of the gas disc. The common low-redshift discs are expected to form predominantly in haloes below the threshold mass of $\sim 10^{12}M_{\odot}$, and not necessarily by narrow streams (Birnboim & Dekel 2003; Binney 2004; Kereš et al. 2005; Dekel & Birnboim 2006; Birnboim et al. 2007). Being gas poor, the low-redshift discs rarely develop axi-symmetric instabilities with $Q < 1$. They can evolve secularly through non-axi-symmetric modes of instability with $Q \gtrsim 1$, associated with quiescent star formation. The turbulent high-redshift discs do not transform into today's thin discs. They end up most naturally in today's thick discs and S0 galaxies, or in ellipticals through mergers.

The above predictions of the simplified theoretical analysis are to be tested below using cosmological simulations. In parallel, the instability analysis will help us interpret the simulated results.

3 THE SIMULATIONS

The simulations that serve as the basis for the current analysis follow the evolution of three typical massive galaxies. They were performed completely independently, not tailored in any way to match the theoretical expectations or the observed SFGs. We selected dark-matter haloes with virial masses $M_{\text{v}} \simeq 10^{12}M_{\odot}$ at $z = 1$, which end up as $(3 - 4) \times 10^{12}M_{\odot}$ today, comparable to and somewhat more massive than the Milky Way. Using the EPS statistic of halo growth (Neistein et al. 2006), the mean virial mass

of the major progenitor of such haloes is expected to be $5 \times 10^{11} M_{\odot}$ at $z \sim 2.3$. The average input rate of gas into such a halo, assuming a universal baryonic fraction of $f_b = 0.165$, is $\dot{M}_b \simeq 6.6 M_{12}^{1.15} (1+z)^{2.25} M_{\odot} \text{ yr}^{-1}$, or $\dot{M}_b \simeq 44 M_{\odot} \text{ yr}^{-1}$ for the haloes in question. These galaxies are thus at the low-mass end of the massive star-forming galaxies in the current surveys, in which the typical halo mass is above $10^{12} M_{\odot}$ and the typical SFR is $\sim 70 M_{\odot} \text{ yr}^{-1}$ (Förster Schreiber et al. 2009). This slight mismatch occurred because these simulations were not originally intended for the particular study reported in the current paper.

The procedure for setting up the initial conditions of the simulations is as follows. We started with a low-resolution cosmological N -body simulation in a comoving box of side $20 h^{-1} \text{ Mpc}$, using the following cosmological parameters suggested by the WMAP5 results (Komatsu et al. 2009): $\Omega_m = 0.27$, $\Omega_{\Lambda} = 0.73$, $\Omega_b = 0.045$, $h = 0.7$ and $\sigma_8 = 0.82$. At $z = 1$, we selected three haloes of $M_v \simeq 10^{12} M_{\odot}$ each, termed A, B and C. The selection was arbitrary, except that we deliberately avoided haloes that were involved in a major merger process at $z \sim 1$. This selection rejected less than 20% of the haloes of that mass and it had no explicit dependence on the merger history prior to $z=1$. One halo (C) happened to be in a relatively dense environment of neighboring haloes, and the other two (A and B) were in a “field” environment, namely part of a typical low-density filament of the cosmic web. These three haloes can therefore be regarded as a small fair sample of the haloes of that mass at that epoch.

For each halo, we identified for re-simulation with high resolution the concentric sphere of a radius twice the virial radius, typically one comoving Mpc. This sphere was traced back to its Lagrangian volume at the initial time, $z = 60$, where we applied a zoom-in technique (Klypin et al. 2001) to refine the fluctuations down to the desired resolution limit. Gas was added to the box following the dark matter distribution with the universal baryonic fraction $f_b = 0.165$. We then re-simulated the whole box, with refined resolution only in the selected Lagrangian volume about the galaxy.

Each simulation has a total of 7×10^6 dark-matter particles, with four different masses. The high-resolution region is resolved with $\sim 4 \times 10^6$ dark-matter particles, each of mass $5.5 \times 10^5 M_{\odot}$. The particles representing stars have a minimum mass of $10^4 M_{\odot}$ and their number increases as the simulation evolves; it reaches a value of $2 - 3 \times 10^6$ stellar particles at $z \simeq 1.3$. The integration of the gravity and the gas physics are performed on an adaptive mesh, where the maximum resolution is 35-70 pc in physical units at all times. This resolution is valid, for example, throughout the cold disc and dense clumps. The numbers characterizing each simulation are summarized in table 1.

The simulations were performed using the ART code (Kravtsov et al. 1997; Kravtsov 2003), following the evolution of the gravitating N -body system and the Eulerian gas dynamics using an Adaptive Refinement Tree. The code incorporates the standard physical processes relevant for galaxy formation, as described in Ceverino & Klypin (2009). These include gas cooling by atomic Hydrogen and Helium, metals, and molecular Hydrogen, photoionization heating by a UV background with proper self-shielding, star

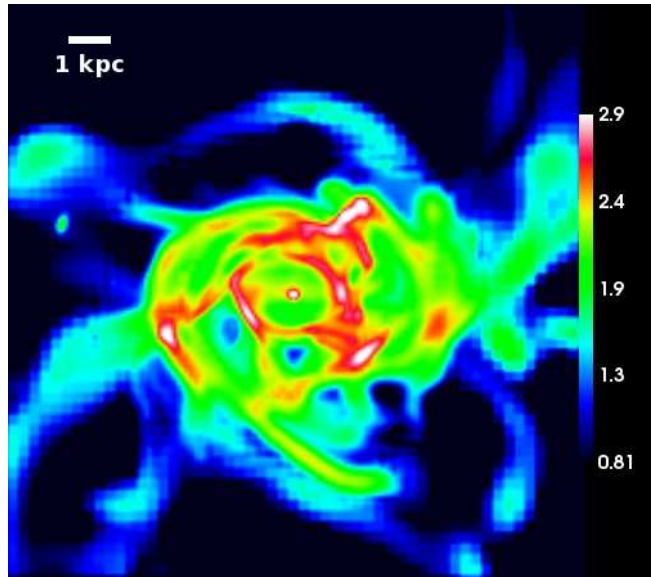


Figure 1. Face-on gas surface density in galaxy C at $z = 2.1$. The image demonstrates violent disc fragmentation into transient features and bound clumps, resembling observed SFGs and theoretical expectations. The size of the image is $15 \times 15 \text{ kpc}$. Surface density is in units of $\log(M_{\odot} \text{ pc}^{-2})$. For comparison, the surface density of molecular clouds in low-redshift galaxies is $\sim 100 M_{\odot} \text{ pc}^{-2}$.

formation, metal enrichment, stellar mass loss, and stellar feedback.

In our stochastic star-formation model, more than 90% of the stars form at temperatures well below 10^3 K and more than half the stars form below 300 K at gas densities higher than 10 cm^{-3} . New stellar particles are generated at every time step of the zero-level grid, which is about 5 Myr at $z = 2$. We use a “constant” feedback model, in which the combined energy from stellar winds and supernova explosions is released as a constant heating rate over 40 Myr , the typical age of the lightest star that explodes as a type-II supernova. The heating rate due to feedback may or may not overcome the cooling rate, depending on the gas conditions in the star-forming regions (Dekel & Silk 1986; Ceverino & Klypin 2009). We also include the effect of runaway stars by assigning a velocity kick of $\sim 10 \text{ km s}^{-1}$ to 30% of the newly formed stellar particles. As a result, these stars can migrate $\sim 100 \text{ pc}$ away from the dense regions and explode as supernovae in regions with lower densities and longer cooling times. This enhances the efficiency of feedback in heating the surrounding gas. Finally, in order to mimic the self-shielding of galactic neutral hydrogen from the cosmological UV background, we assume that in regions where the gas density is higher than $n = 0.1 \text{ cm}^{-3}$, the ionizing flux shrinks to a negligible value (i.e., $5.9 \times 10^{26} \text{ erg s}^{-1} \text{ cm}^{-2} \text{ Hz}^{-1}$, the value of the pre-reionization UV background at $z = 8$).

4 GLOBAL PROPERTIES AT HIGH REDSHIFT

Our analysis here focuses on the three simulated galaxies at $z \sim 2-2.5$, when the Universe was roughly 3 Gyr old. These redshifts are in the middle of the redshift range $1.5-3$ where

Table 2. Global properties of the host haloes at redshift $z = 2.3$. Radii are expressed in proper kpc, masses in units of $10^{11}M_{\odot}$ and velocities in km s^{-1} .

Galaxy	R_v	M_v	V_v
A	70	4	150
B	68	3.5	140
C	83	6.1	180

the activity of disc instability and star formation is expected to be at its peak, both according to observations of SFGs and the predictions of DSC. Figure 1 presents the gas surface density in galaxy C at $z = 2.1$. The face-on view angle is defined by the angular momentum of the $T < 10^4\text{K}$ gas inside a sphere of 3 kpc. The image shows an extended disc of diameter ~ 9 kpc and the 70 pc resolution reveals that the disc is highly perturbed, with a few big, round clumps embedded in massive elongated tangential features. The elongated structures are transient features being disrupted by shear. The clumps are bound, with typical masses $\sim 10^8M_{\odot}$ and characteristic sizes ~ 1 kpc. About 10 – 20% of the total mass of the disc is in the clumps and sheared features. This galaxy, like the other two, also has a stellar bulge, of mass comparable to the overall disc mass. The very clumpy appearance of this high-redshift disc and its massive bulge, which repeats in the other two simulated galaxies, is revealed for the first time in cosmological simulations. A first visual inspection indicates that it resembles the clumpy appearance of the typical observed SFGs, and follows the theoretical expectations laid out by DSC, §2.

Before we proceed to analyze the detailed properties of the simulated clumpy discs and bulges in comparison with the observed SFGs and the theoretical predictions, we address the main global properties of the dark-matter haloes and the stellar components in the simulated galaxies. We wish to verify in particular that they are consistent with the observed global properties of high-redshift star-forming galaxies, and their main scaling relations.

4.1 Virial Properties of the Dark-Matter Haloes

Table 2 displays the virial properties of the simulated haloes at $z = 2.3$. The virial radius R_v and the corresponding mass M_v are defined to encompass a mean mass density of 180 times the universal mean, and the virial velocity is $V_v \equiv (GM_v/R_v)^{1/2}$. Haloes A and B are similar, with $M_v \simeq 4 \times 10^{11}M_{\odot}$ and $V_v \simeq 150 \text{ km s}^{-1}$, while halo C is a bit more massive with $M_v = 6 \times 10^{11}M_{\odot}$ and $V_v = 180 \text{ km s}^{-1}$.

Galaxy C has a growth history that differs from the other two. By $z = 2.3$, its halo has already assembled about half the mass that it will have at $z = 1$, while haloes A and B have assembled only a quarter of their $z = 1$ mass. The growth of C is thus faster prior to $z = 2.3$, and the growth of the other two is more rapid after $z = 2.3$. This reflects the fact that halo C was forming in an environment of higher density. The cosmological overdensity of matter in a concentric sphere of comoving radius $5 h^{-1}\text{Mpc}$ about haloes A and B at $z = 2.3$ is only $\delta\rho/\rho \simeq 0.07$ and 0.02 respectively, while it is as high as $\delta\rho/\rho \simeq 0.3$ for halo C. This difference, representing the “cosmic variance”, was set by our selection of haloes. We will see that the cosmic environment plays an

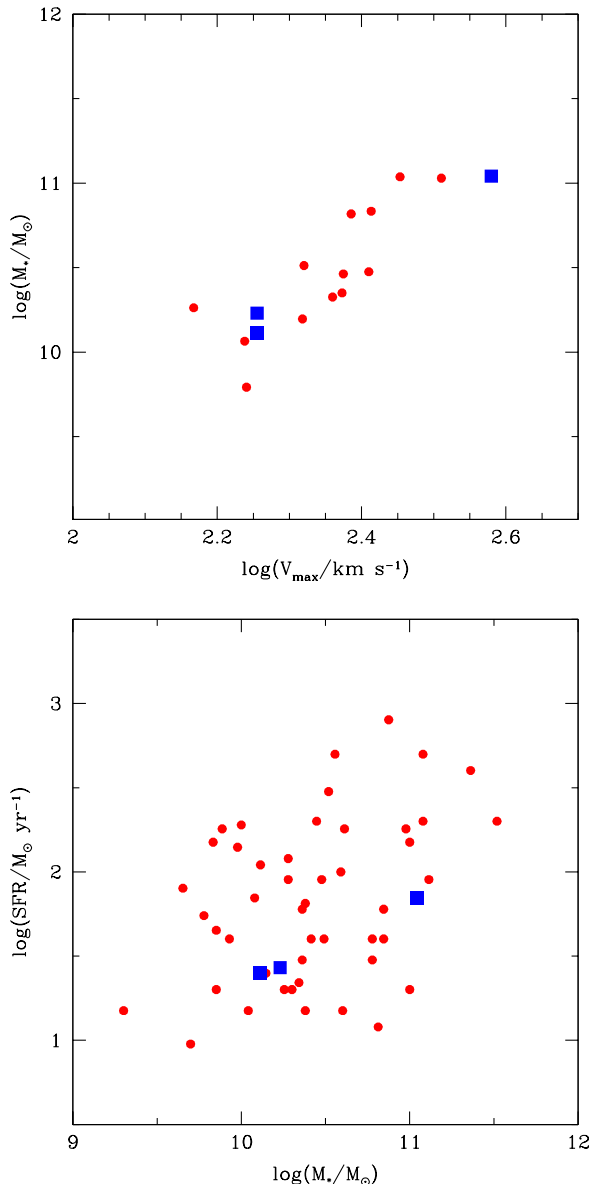


Figure 2. Scaling relations at $z \sim 2.3$ for our three simulated galaxies (blue squares) in comparison to observed galaxies (red circles). Observations are from the SINS survey (Förster-Schreiber et al. 2009; Cresci et al. 2009). The top panel shows the Tully-Fisher relation, stellar mass versus maximum rotation velocity. The bottom panel shows the “main sequence” of star-forming galaxies, SFR versus stellar mass. The simulated galaxies seem to obey the observed scaling relations within the given scatter. They lie near the best-fit line of the Tully-Fisher relation, but they have SFR values about a factor of two lower than the average value for their stellar mass.

important role in the formation of galaxies at the centres of these haloes, especially because the earlier formation time of halo C makes it denser in its central regions, both in dark matter and in gas.

4.2 Scaling Relations at High Redshift

Figure 2 refers to the two main scaling relations of SFGs, correlating the total stellar mass to SFR and to disc rotation

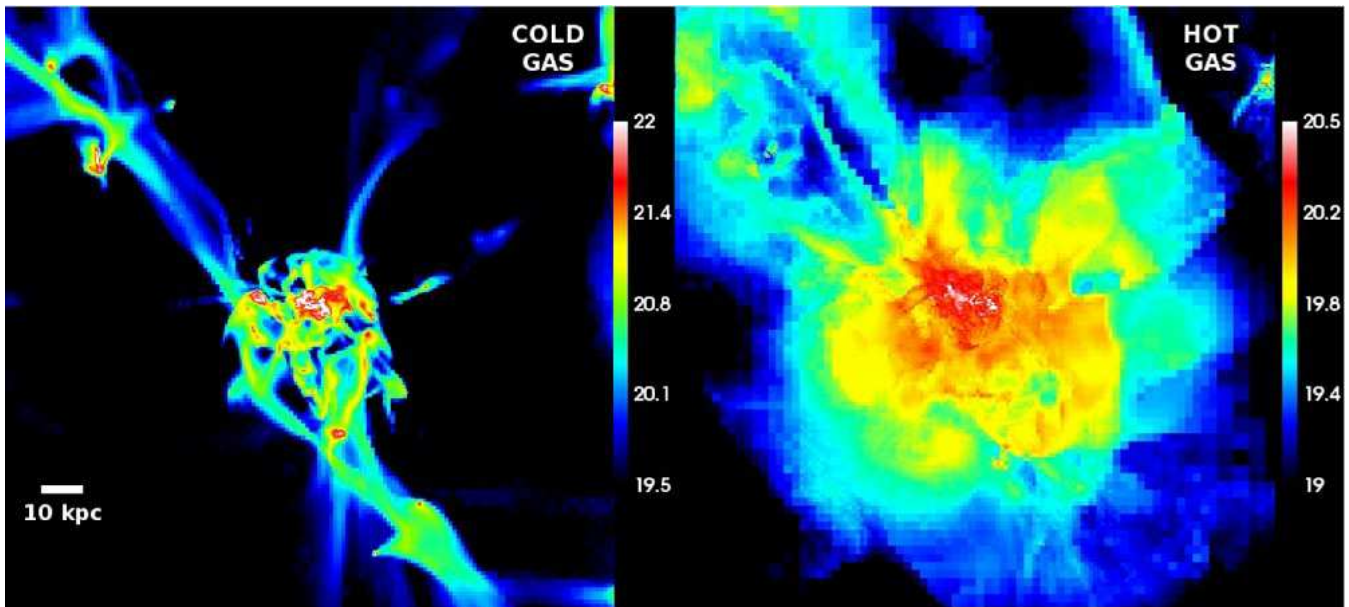


Figure 3. A zoom-out gas surface-density maps showing the streams feeding galaxy A. Left: cold gas ($T < 5 \times 10^4$ K). Right: hot gas ($T > 3 \times 10^5$ K). The box size is 160×160 kpc, covering the whole virial sphere. The color refers to log gas surface density in units of H atoms cm^{-2} . Two major narrow streams carry the gas from well outside the virial radius to the inner ~ 20 kpc halo core, where they break into a multi-stream turbulent core before joining the inner disc of radius ~ 6 kpc, seen nearly edge-on at the box centre (mostly in white).

velocity. The observational data is extracted from the SINS survey (Förster Schreiber et al. 2009) — a spectroscopic imaging survey in the near-infrared with SINFONI/VLT that focuses on SFGs at $z \sim 2$.

The top panel of figure 2 puts our simulated galaxies in the context of the Tully-Fisher relation. The observational data is taken from the SINS sample of disc galaxies (Cresci et al. 2009). Since the rotation curves in the simulated galaxies are rather flat outside the bulge, we adopt the average rotation velocity in the gaseous disc as our estimate for V_{max} (see §5.4). The simulated galaxies seem to follow quite well the observed Tully-Fisher relation.

The bottom panel addresses the “main sequence” of star formation, namely the SFR as a function of total stellar mass. Given the scatter, the three simulated galaxies are consistent with the observed relation. The fact that they lie a factor of ~ 2 below the mean SFR at a given mass may be a random coincidence or it may reflect a certain deficiency in the simulated star-formation history. The stellar masses in A and B are at the level of 5% of their halo masses of $\sim 4 \times 10^{11} M_{\odot}$, which is quite typical for such haloes. The SFR in these galaxies are comparable to and only slightly smaller than the expected average gas accretion rate into haloes of similar masses, $\sim 30 M_{\odot} \text{yr}^{-1}$. In galaxy C, with a halo only slightly more massive but a significantly denser environment and an earlier growth, the stellar mass is higher than average, and the SFR is higher than the average accretion rate.

The agreement with the Tully-Fisher relation may indicate that the small systematic deviation in the SFR- M_{\star} relation reflects a deficiency in the current SFR at $z = 2.3$ rather than in stellar mass. It is thus possible that the simulated galaxies overproduce stars prior to $z \sim 2.3$, and then underestimate the gas fraction and the SFR at $z \sim 2.3$, while they reproduce the proper stellar mass. This may result, for example, from slightly underestimating the effect

of supernova feedback at high redshifts. Indeed, the SFR, and how it is affected by stellar and supernova feedback, are naturally the most uncertain elements in our simulations, as these processes are implemented via crude recipes of subgrid physics. Despite this potential small deficiency, we conclude that the simulated galaxies do obey in a satisfactory way the main observed scaling relations, so their global properties can be considered as representative of typical SFGs of a similar mass at a similar time.

5 CLUMPY DISCS AND BULGES IN STEADY STATE

5.1 Feeding by Cold Streams

Figure 3 shows a virial-scale view of the gas surface-density in halo A. The cold gas, $T < 5 \times 10^4$ K, flows along narrow streams that come from outside the virial radius and penetrate to the centre of the dark-matter halo. There, they blend in the inner ~ 20 kpc into a turbulent region and eventually settle in a clumpy disc of radius ~ 6 kpc. The shock-heated gas of $T > 3 \times 10^5$ K fills much of the virial sphere. In the disc vicinity, the hot gas is also clumpy, perhaps indicating the presence of shocks at the interfaces between the streams and the central galaxy.

5.2 Images of Gas, Stars and Dark Matter

Figures 4-6 show face-on and edge-on views of the galaxies in the inner $\sim 10\%$ radius of the three haloes at $z = 2.3$. The maps display on the same scale the distribution of gas, SFR, stars and dark matter.

Figure 4 refers to galaxy A. The gas surface density maps show a thick disc of radius ~ 6 kpc and thickness ~ 1 kpc. The disc is highly fragmented showing several giant

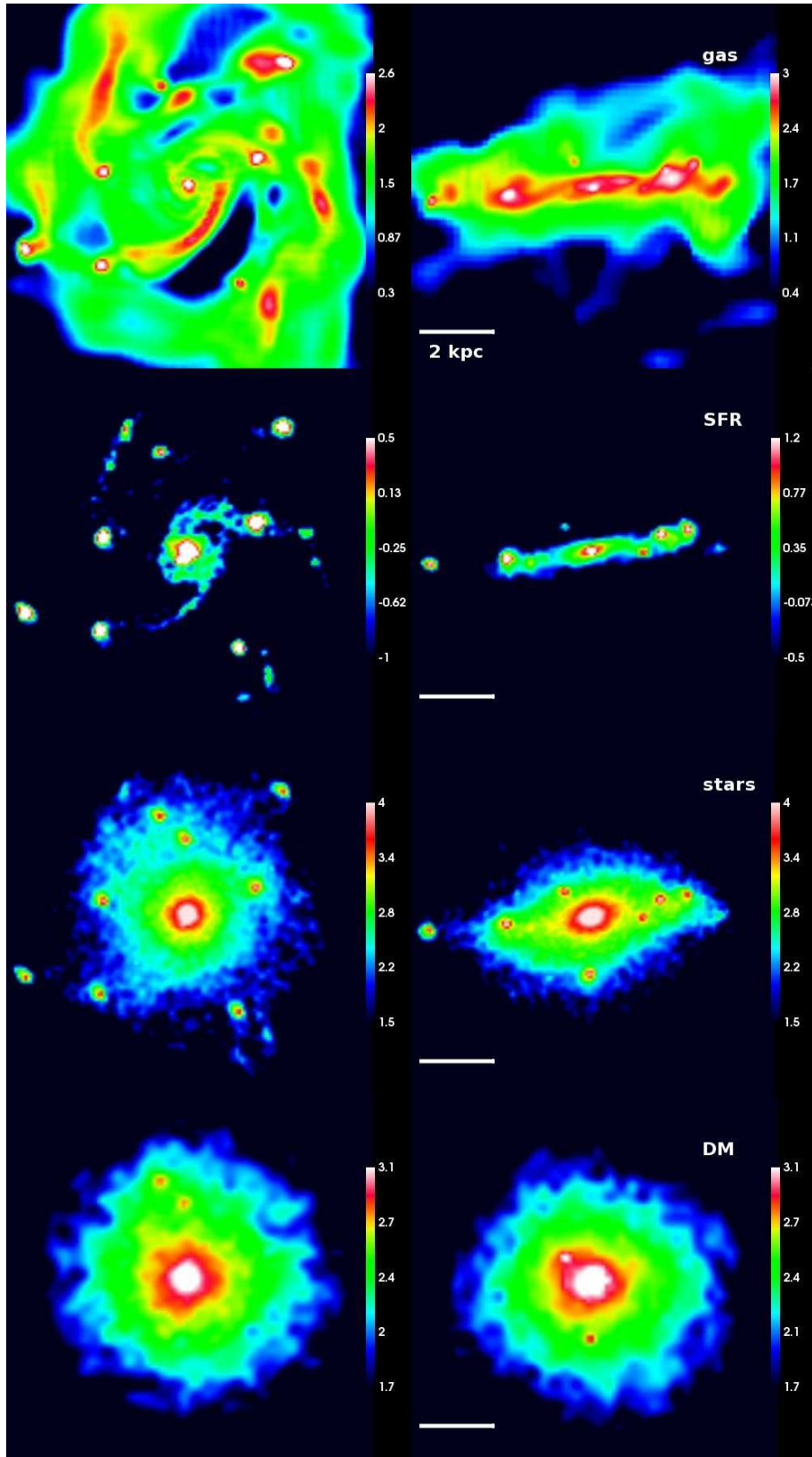


Figure 4. Surface density maps of galaxy A at $z = 2.3$. The side of each panel is 10 kpc. Shown are face-on views (left) and edge-on views (right). From top to bottom: gas, SFR, stars, and dark matter. The units are $\log(M_{\odot} \text{pc}^{-2})$ for the surface density and $\log(M_{\odot} \text{yr}^{-1} \text{kpc}^{-2})$ for the SFR. We see a disc of gas and young stars, a significant bulge extending to a very thick disc of old stars, and a rather spherical dark-matter halo. The disc is fragmented to elongated features and round dense clumps. Stars form at a high rate in the clumps and at the centre of the bulge. Most of the clumps are in-situ to the disc and are not associated with dark-matter concentrations. Two of the clumps are off-disc satellites. The color code was chosen to emphasize the clumps at the expense of saturating the highest densities.

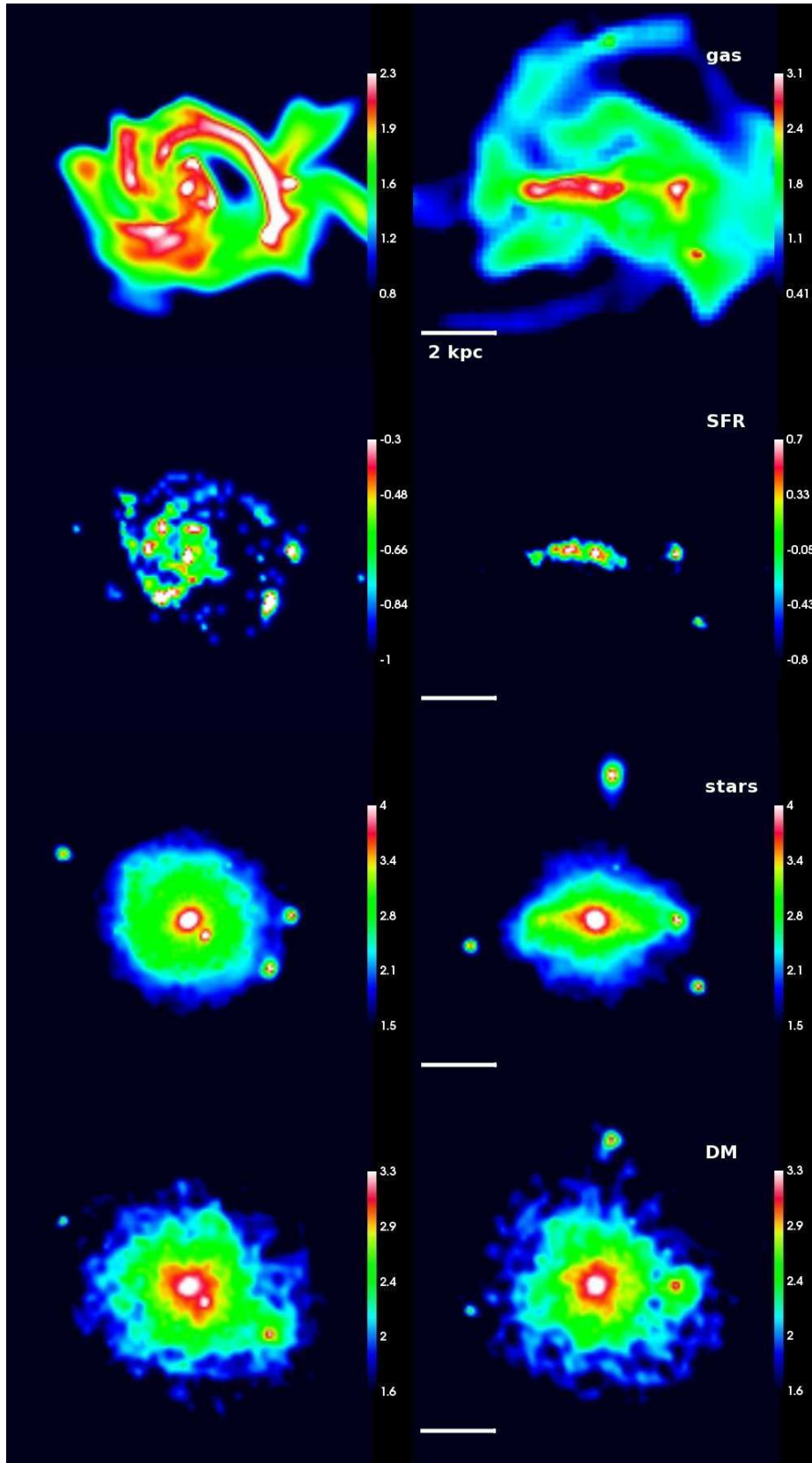


Figure 5. Same as in figure 4 but for Galaxy B. This case shows the smallest disc of the sample. Beyond the high SFR in clumps, there is a relatively high SFR in other regions spread across the disc, some associated with the elongated transient features. The overall stellar population is rather smooth and concentrated in the bulge. Two clumps are external satellites with stars and dark matter.

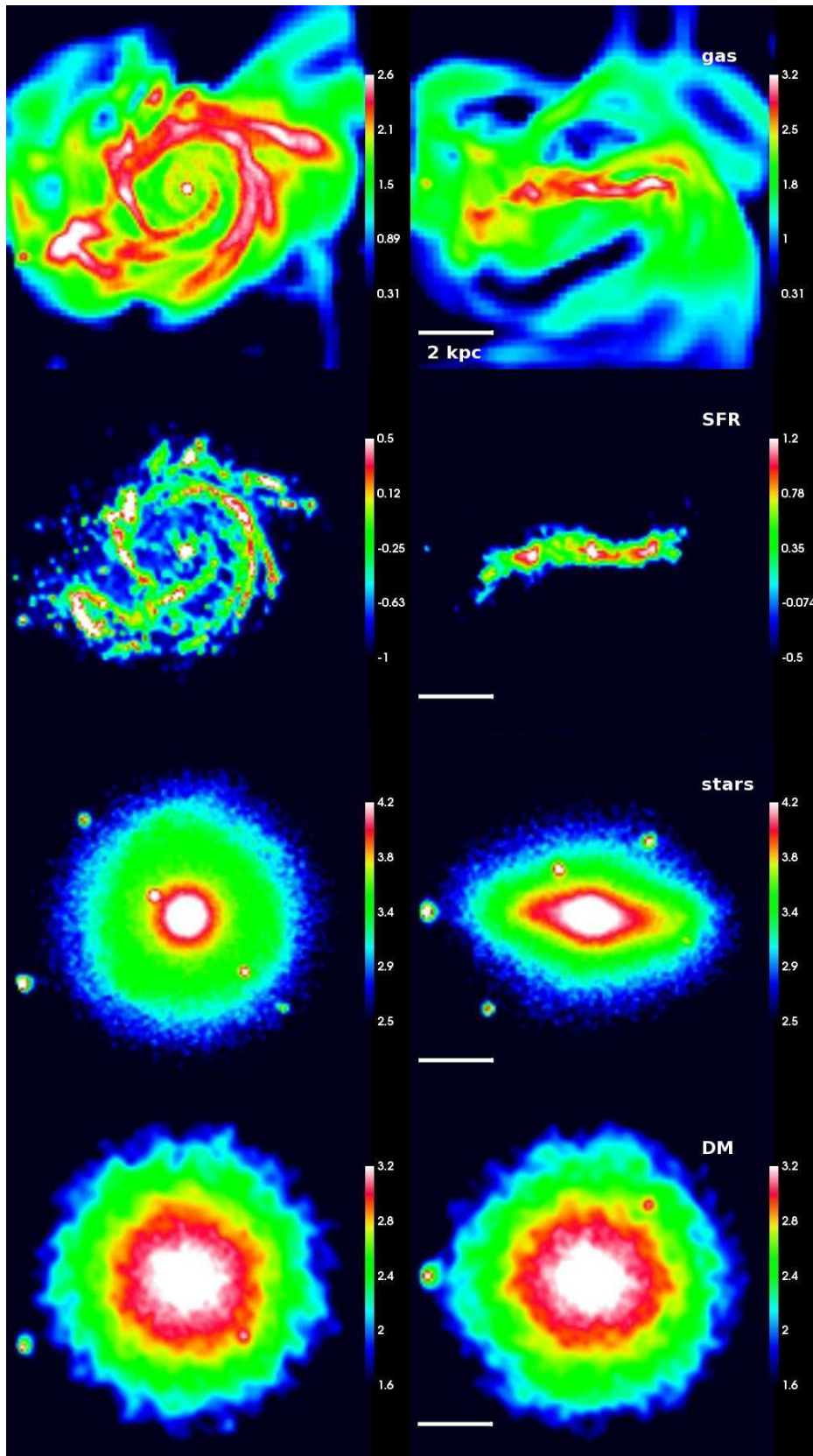


Figure 6. Same as in figure 4 but for Galaxy C. This is the most massive and early forming galaxy in our sample. It has the highest surface densities of gas and stars and is therefore highly unstable. Star formation occurs in an extended clumpy ring. Two clumps are external, with stars and dark matter.

clumps and elongated transient clouds as in Figure 1. The SFR, as deduced from the stars younger than 10 Myr, reveals that a large fraction of the stars form in the disc clumps and in the centre of the bulge. The stars show a thick disc with embedded clumps, all associated with the gas, star-forming clumps, but the stellar distribution is dominated by a massive bulge, of a mass comparable to the disc mass. The bulge extends to a very thick disc, perhaps resembling a lenticular galaxy. The dark-matter distribution is rather spherical and smooth, with only two obvious dark-matter satellites, both off the disc plane. The disc clumps are thus all naked, not associated with small dark-matter haloes of their own. This is evidence for the in-situ nature of the disc clumps, indicating that they were originated in the disc itself rather than merged as small galaxies coming from the outside along the streams. The two off-plane satellite galaxies have haloes of masses $10^8 - 10^9 M_\odot$ and eccentric orbits that lead them to future mergers with the bulge while they never become part of the rotating disc.

Figure 5 shows galaxy B. This galaxy, in the smallest halo of the three, has a disc radius of only ~ 3.5 kpc. The gaseous disc is strongly perturbed, with clumps embedded in elongated massive features that resemble spiral arms. The gas clumps here are less compact than in galaxy A, with a lower surface density extending to larger radii. The low stellar fraction in these clumps, compared to the clumps of galaxy A, reflects the transient nature of these features. The overall SFR of $\sim 30 M_\odot \text{yr}^{-1}$ is similar to galaxy A but it is spread over the clumps and the broad elongated features covering a large fraction of the disc. The dark-matter map shows two satellites, coinciding with two clumps of gas and stars, of which one is actually in the disc plane. All the other clumps and elongated features are in-situ to the disc and not associated with dark-matter substructures. A non-negligible stellar bulge is seen, with a mass comparable to the disc mass, but it is less massive than in the other two cases.

Figure 6 displays galaxy C, the most massive case that assembled most of its dark matter and accreted most of its baryons earlier than the other two. The gas disc is very clumpy and disturbed, despite the relatively low gas fraction of less than 10% in this galaxy. The instability is largely because the disc is more massive and more compact than in the other cases, with a high surface density in both gas and stars, $\sim 2 \times 10^2$ and $3 \times 10^3 M_\odot \text{pc}^{-2}$ respectively. The clumps and elongated features display a star-forming ring outside the bulge. This structure is remarkably similar to observations of star-forming outer rings in some $z \sim 2$ galaxies (Genzel et al. 2008). Two off-plane satellites are seen in the stars, of which at least one is clearly associated with a dark matter satellite. The main features in the disc are not associated with dark-matter substructure. As in the other two cases, the bulge is as massive as the disc.

In general, all three cases show a gravitationally unstable, extended, thick and irregular disc, with massive in-situ clumps and transient features, accompanied by a compact bulge of comparable mass, consistent with observations and the cosmological steady state predicted by theory. The mean gas surface density within the clumps is high, $\Sigma_g \sim 500 - 1000 M_\odot \text{pc}^{-2}$, compared to the typical values of $\sim 100 M_\odot \text{pc}^{-2}$ in the “giant” molecular clouds in low-redshift galaxies (Bolatto et al. 2008; Heyer et al. 2008). This allows high, starburst-like,

SFR surface densities of $\sim 10 M_\odot \text{yr}^{-1} \text{kpc}^{-2}$, as expected from the Schmidt-Kennicutt relation (Kennicutt 1998). Overall, 10 – 20% of the gas in the discs is in the form of clumps and sheared features. They are larger and much more massive than the star-forming molecular complexes in quiescent, low-redshift disc galaxies. This makes the gravitational interaction between the clumps and the transient features more intense, resulting in high turbulence and rapid mass flow to the center. The surface density in the transient clouds is $(100 - 500) M_\odot \text{pc}^{-2}$ and they are embedded in a smoother inter-clump medium of surface density $\sim 30 M_\odot \text{pc}^{-2}$.

5.3 A Preliminary Comparison with Observed Images

k

In Fig. 7 we show side by side images of simulated and observed galaxies, as a sneak preview for a quantitative comparison to be provided elsewhere (Ceverino, Bournaud & Dekel 2009, in prep.). Edge-on and face-on images of simulated galaxy A at $z = 2.3$ are shown next to a “chain” and a “clump-cluster” galaxy respectively. Since the young stars contribute a significant fraction of the rest-frame U-band luminosity, the images of simulated stars younger than 100 Myr are compared to observed UV rest-frame images from the Hubble Ultra Deep Field (HUDF). The mean rest-frame UV (observed i band at $z=2.3$) mass-to-light ratio of the simulated stellar population is $0.1 M_\odot/L_\odot$, according to GALAXEV population synthesis code (Bruzual & Charlot 2003) The pixel size and seeing are assumed to be 0.11 and 0.5 kpc, respectively. Galaxy A is shown at $z = 2.3$ because this is near where the clumpy appearance peaks in this particular simulation. The chosen UDF galaxies are at $z = 3.3$ and $z = 1.3$ respectively and they bracket our fiducial model at $z = 2.3$. This is fine for a very qualitative visual comparison given the observational evidence for a similar clumpy morphology of observed star-forming galaxies across the redshift range $z = 1 - 4$ (e.g., Elmegreen et al. 2007). The weak sensitivity to redshift is also consistent with the analytic prediction by DSC of a cosmological steady state. Therefore, for this very qualitative visual comparison, we did not make an effort to fully match redshifts, luminosities, masses and other galaxy properties, except for the overall similarity of disk size and the clumpy nature of the young stellar population. A visual comparison indicates that the general morphological features of the high-redshift clumpy SFGs are successfully reproduced by our simulations. At least in the specific cases shown, the similarity includes the number and sizes of clumps, their distribution throughout the system, and the contrast between the clumps and the inter-clump medium. This preliminary comparison is for illustrative purposes only — it is neither meant to provide a detailed modeling of the two specific galaxies, nor to present a statistically significant comparison of fair samples.

The dominance of a few giant clumps is a common feature to the simulated and observed galaxies. For example, in galaxy A, about 40% of the young stars are in the in-situ disk clumps, and 10% in the bulge. The inter-clump medium, which is naturally more evident in the edge-on views, is the site for the other half of the SFR, which is associated with diffuse inter-clump UV light. This is consistent with

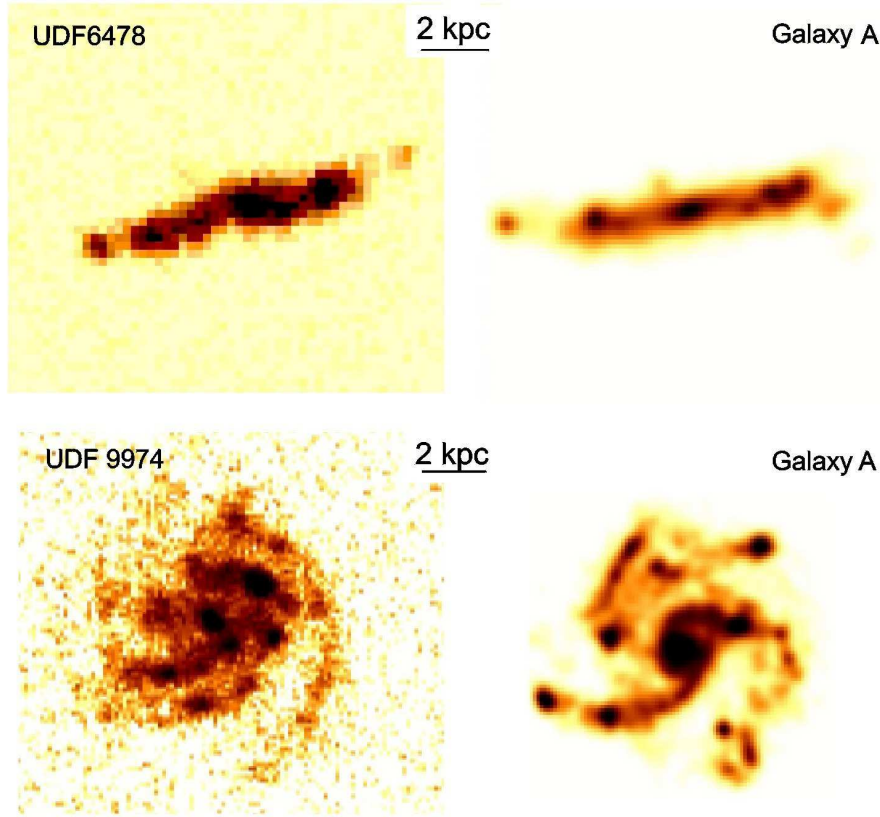


Figure 7. Typical images of observed and simulated clumpy disks at high redshifts. Left: UV rest-frame surface brightness of two galaxies from the Hubble Ultra Deep Field, representing the different appearances of the clumpy discs depending on the viewing angle: a “chain” galaxy (UDF 6478, z-band at $z = 3.3$) and a face-on “clump cluster” (UDF 9759, V-band at $z = 1.2$). The 3σ sensitivity in the images is $25.5 \text{ mag arcsec}^{-2}$ and the surface brightness of the brightest clump (in black on the images) is around $21 \text{ mag arcsec}^{-2}$. Right: The simulated galaxy A viewed at $z = 2.3$ with about the same resolution, using as a proxy for the UV emission the stars younger than 100 Myr. The maximum and minimum surface densities are 0 and 4 in $\log(M_{\odot} \text{pc}^{-2})$. The color code is logarithmic and the same for the observations and the simulations. The pixel size and seeing are assumed to be 0.11 and 0.5 kpc, respectively. We do not aim here at modeling individual galaxies or making a valid statistical comparison between the simulated and observed morphology. We pick the observed galaxies at redshifts that bracket our fiducial simulation at $z = 2.3$, and because there is observational evidence for a similar morphology in the redshift range $z = 1 - 4$ (e.g., Elmegreen et al. 2007). A visual comparison indicates that our simulations may reproduce the key morphological properties of high-redshift clumpy galaxies.

the observation that $\sim 30\%$ of the light in cluster galaxies is coming from clumps (Elmegreen et al. 2005b). The clump sizes, their contrast with the rest of the disc, and their spatial distribution throughout the system, all seem strikingly similar between simulation and observation. In particular, some of the simulated galaxies show asymmetric configurations, resembling the observed “tadpole” galaxies. The mean stellar age within individual clumps, averaged over all the clumps of galaxy A, is ~ 80 Myr. The dispersion of stellar ages within a clump is comparable, ~ 70 Myr. This implies that the star-formation history within each clump is continuous over a period of $100 - 200$ Myr. These stellar ages are similar to the age estimations from observations (Elmegreen et al. 2009). The mean stellar ages within the bulge is ~ 1 Gyr, with a spread of ~ 0.5 Gyr, in agreement with the observational estimates (Elmegreen et al. 2009).

All three simulated galaxies host central stellar bulges with masses comparable to the disc mass, in agreement with the estimated bulge-to-total mass ratio from the SFGs at high redshift (Genzel et al. 2008; Elmegreen et al. 2009). These stellar spheroids are rather compact, with radii ($1 - 2$) kpc,

compatible with the spheroids detected at high redshifts (Kriek et al. 2006; van Dokkum et al. 2008; Bezanson et al. 2009).

5.4 Galaxy Properties vs Theory and Observation

Table 3 lists global properties for the main components of the three galaxies: cold gas ($T < 10^5$ K), stars and dark matter inside the disc radius, R_d . This radius is estimated from a visual inspection of figures 4-6 and the associated density profile of the stellar and gas disc, which are both truncated at a similar radius. The bulge radius R_b is read quite straightforwardly from the stellar density profile, which shows a well defined transition from a steep inner profile characteristic of a bulge and a shallower outer exponential profile with an exponential radius of $1 - 2$ kpc, comparable to the bulge radius. The density profile of the gas disc is much shallower, with an exponential radius comparable to the outer disc radius R_d .

We use the kinematics of the star particles to distinguish the stellar disc from the spheroidal component. We assign

Table 3. Galaxy properties at $z = 2.3$. Radius in kpc and mass in $10^{10}M_{\odot}$.

Galaxy	R_{disc}	R_{bulge}	M_{gas}	M_{stars}	M_{DM}	M_{bulge}	M_{disc}	$M_{\text{disc}}/M_{\text{total}}$	$M_{\text{gas}}/M_{\text{disc}}$	$M_{\text{bulge}}/M_{\text{disc}}$	$M_{\text{clumps}}/M_{\text{disc}}$
A	5.8	2.0	0.37	1.73	2.1	1.0	1.1	0.26	0.35	0.93	0.14
B	3.4	1.0	0.20	1.27	0.92	0.81	0.66	0.27	0.30	1.22	0.24
C	4.6	1.5	0.46	11.44	3.4	6.6	5.3	0.35	0.09	1.25	0.15

Table 4. Star formation and baryonic fraction. SFR in $M_{\odot} \text{yr}^{-1}$, star-forming gas mass in $10^{10} M_{\odot}$, and star-formation time in Myr.

Galaxy	SFR	$M_{\text{SF-gas}}$	t_{SF}	$M_{\text{galaxy}}/M_{\text{v}}$
A	27	0.21	78	0.052
B	25	0.13	52	0.042
C	70	0.33	47	0.19

a star particle to the disc only if the z -component of its angular momentum j_z (parallel to the total galaxy angular momentum) is higher than a fraction f_J of the maximum angular momentum for the same orbital energy, $j_{\text{max}} = |v| r$, where $|v|$ is the magnitude of the particle velocity and r is its distance from the center. The distribution of j_z/j_{max} among the simulated stars is bimodal, reflecting the division to distinct kinematic components of disc and bulge. We adopt as default $f_J = 0.7$, which roughly marks the transition between the two components of this distribution. We thus define the bulge mass, M_{bulge} , as the mass in stars inside R_{d} with $j_z/j_{\text{max}} > f_J$, and the disc mass, M_{disc} , as the mass of cold gas, M_{gas} , plus the mass in stars with $j_z/j_{\text{max}} > f_J$.

We find in the three galaxies values of $\delta \sim 0.3$ for the disc-to-total mass ratio (eq. (4)). These are compatible with the values predicted by DSC for unstable discs in cosmological steady state. The simulations thus reveal the predicted even distribution of mass between the disc, bulge and dark-matter components within the disc radius.

The gas fractions in the discs of A and B are 35% and 30% respectively. This is significantly higher than in today’s typical spirals, where the gas fraction is typically $\sim 10\%$ or less. It is comparable, and perhaps on the low side of the crude observational estimates for typical high-redshift SFGs, both the indirect estimates based on the Kennicutt-Schmidt relation (Erb et al. 2006; Genzel et al. 2006) and the direct estimates based on CO observations (Daddi et al. 2004; Greve et al. 2005; Tacconi et al. 2006, 2008; Daddi et al. 2008, 2009). The gas fraction in galaxy C is lower than 10%, making it atypical. This may reflect an overproduction of stars too early in this simulation (see §7). The baryonic fractions within the disk radius in the three simulated galaxies, 0.5, 0.87, and 0.77, are consistent with the observational estimates (Förster Schreiber et al. 2009, Fig. 20). The fact that the gas fractions are lower than expected should be taken into account in the instability analysis, but it is encouraging to note that the clumpy appearance of the discs, and even the values of δ as derived from the combined disc of gas plus stars, are consistent with the observations and the theoretical predictions.

Assigning gas to clumps using a density threshold of $n = 25 \text{ cm}^{-3}$ (or any value in the range $(10-40) \text{ cm}^{-3}$), we obtain that the fraction of the disc in clumps is $0.15 - 0.25$.

Table 5. Kinematic disc properties. Velocities are in km s^{-1} .

Galaxy	V_{gas}	$\sigma_{r,\text{gas}}$	$(\sigma_r/V)_{\text{gas}}$	V_{stars}	$\sigma_{r,\text{stars}}$	$(\sigma_r/V)_{\text{stars}}$
A	180	20	0.11	160	33	0.22
B	180	25	0.14	157	34	0.26
C	380	60	0.16	356	107	0.30

Indeed, these fractions in clumps are consistent with the value of $\alpha \sim 0.2$ adopted in the analysis of DSC. The mean clump mass in all cases is $\sim 10^8 M_{\odot}$, in agreement with the prediction, eq. (2). The clump radius ranges from 0.2 to 1 kpc, consistent with the pre-collapse radius predicted in eq. (3) for galaxies of such mass, $R_c \sim 0.8 \text{ kpc}$. The bound clumps, as opposed to the transient features, have rather sharp boundaries, and they are approximately in virial equilibrium.

Table 4 lists galaxy properties that are related to star formation (discussed in section 4.2) and baryonic fraction. The average SFR of $45 M_{\odot} \text{yr}^{-1}$ is in the ballpark of the expected mean gas accretion rates, eq. (7), with the SFR in galaxy C slightly above the average. This is consistent with the main finding of Dekel et al. (2009), based on a large hydrodynamical cosmological simulation, that a few cold streams carry almost all the accreted gas into the inner galaxy where it turns into stars in a rate comparable to the accretion rate. In order to estimate the timescale for star formation, or for gas consumption, we compute the mass of “star-forming gas”, $M_{\text{SF-gas}}$, inside the disk radius R_{d} . We define this as the gas with a density higher than 1 cm^{-3} and a temperature lower than 10^4 K . It represents 60-70% of all the gas in the disc. The ratio between the star-forming gas and the SFR defines a SFR timescale of $t_{\text{SF}} = 50 - 80 \text{ Myr}$, which is somewhat shorter than estimated from observed galaxies at high redshift (Förster Schreiber et al. 2009).

Two of the simulated galaxies show a low mass fraction of galactic baryons inside the dark-matter halo, which is 25-32% of the cosmological baryonic fraction f_b , probably reflecting gas outflows from the small building blocks of these galaxies. These values are in accord with the baryonic fractions that are estimated for massive, present-day galaxies (F. Prada, private communication). The baryonic fraction in galaxy C is high, and it may reflect an exceptionally high baryonic accretion-rate history.

Table 5 summarizes the global kinematics properties of the gaseous and stellar disc: the rotational velocity, V , and the radial velocity dispersion, σ_r . These quantities are the density-weighted mean values for the disc outside the bulge, $r > R_b$, where the rotation curve is roughly flat. The stellar disc is defined using the kinematic method described above. Galaxies A and B show similar overall kinematics. Their rotational velocity of $V \simeq 160 \text{ km s}^{-1}$ is comparable

to that of today’s discs in similar haloes. However, their velocity dispersion of $\sigma_r \simeq 30 \text{ km s}^{-1}$ is higher than in today’s discs, reflecting a thick and irregular disc in which the pressure is dominated by turbulence. Within the clumps, the internal gas velocity dispersion is $\sim 20 - 30 \text{ km s}^{-1}$, and here too it is the dominant source of pressure. Galaxy C is again different; its rotational velocity and dispersion are significantly higher than in the other two cases. The σ_r/V ratio for the gas in the three cases is between 0.1 and 0.2, in agreement with the theoretical expectation, eq. (5), which is $\sigma_r/V = 0.12 - 0.17$ for $\delta = 0.3$ and $Q_c = 0.67 - 1.0$. These values are compatible with the observed high-redshift discs (Genzel et al. 2006; Förster Schreiber et al. 2009) and are significantly higher than in low-redshift discs.

5.5 Gravitational Instability

Figure 8 displays face-on maps of the local effective Q parameter, computed following eq. (8) assuming a two-component disc of gas and stars. At each point in the disc, we used eq. (1) separately for each component to compute Q_g and Q_s from the corresponding values of Σ and σ_r and the common value of Ω . One can see that in all cases, a significant fraction of the disc is unstable with $Q < 1$. These fractions are 33%, 21% and 13% for A, B and C respectively. We also note that in galaxies A and B the most unstable regions define extended rings, similar to the rings of star formation observed in some of the SFGs (Genzel et al. 2008).

The interpretation of the Q values obtained here from the simulated discs is not straightforward because they were measured from the highly perturbed discs while the linear analysis refers to the slightly perturbed disc at the onset of instability. We see that while the regions where $Q < 1$ naturally include all the dense clumps and transient perturbations, they also extend to regions that seem less perturbed, probably on their way to develop nonlinear perturbations.

Galaxy A is the “most unstable” case, reflecting its high gas fraction and its low rotational velocity. Galaxy C is the most stable case, with a low gas fraction and a high rotational velocity. Still, galaxy C develops the most pronounced sheared features of the sample. About 60-70% of each disc have a Toomre parameter $Q < 2$, capable of developing high-order instabilities. It is interesting to note that these discs are highly unstable despite the dominance of the stellar component. As expected from eq. (8), the stellar component of the disc contributes to the local self-gravity that drives the instability, and helps destabilizing the disc.

5.6 Evolution of Clumps and Spheroid Growth

Figure 9 follows the formation of an individual clump in the disc of galaxy A near $z \simeq 2$. It starts from a small-amplitude perturbation in a rather smooth region of the outer disc. During the initial 10 Myr, it is tangentially elongated due to shear. By 30 Myr it has turned into a high-contrast, round, bound and virialized clump. This is comparable to the dynamical time of this disc, $t_d = R_d/V \simeq 31 \text{ Myr}$, or the free-fall time for a medium of $n \simeq 4 \text{ cm}^{-3}$.

Some of the features seen in these images are transients,

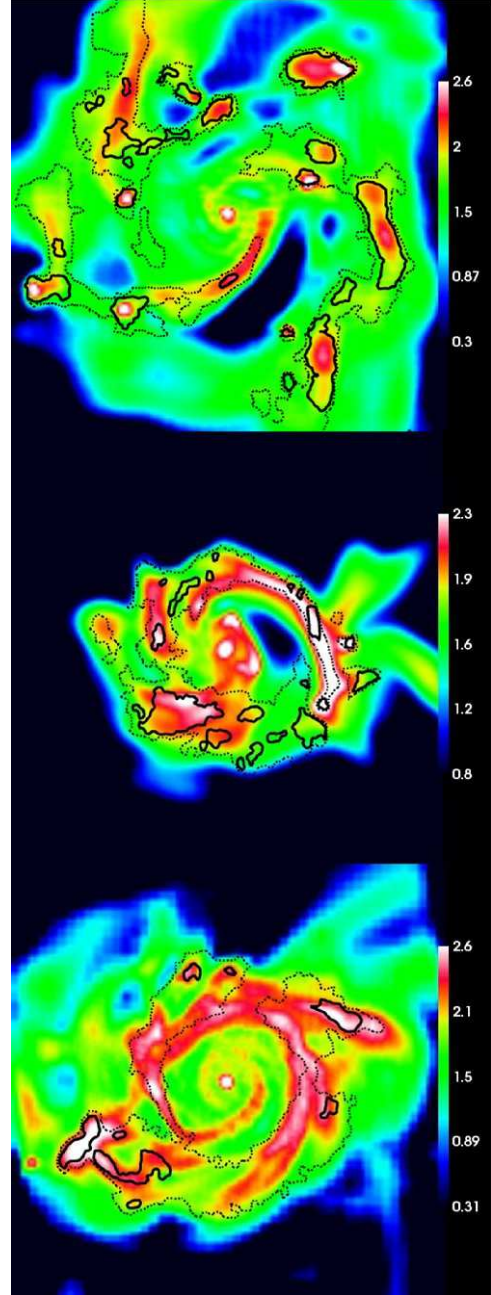


Figure 8. Instability analysis. Shown are maps of the effective Q parameter in the discs of galaxies A (top), B (middle) and C (bottom) overlapped over the gas surface density maps of figures 4, 5 and 6. The value of Q is computed from eq. (8) assuming a two-component disc. The inner, solid contour refers to $Q = 1$, and the outer, dashed contour to $Q = 2$. In all cases, a significant fraction of the disc has $Q < 1$, so it is gravitationally unstable for axis-symmetric modes. The larger regions where $1 < Q < 2$ can be subject to higher modes of instability.

where the strong shear prevents gravitational collapse. Such a transient can be seen in the bottom panels, rotating from left to top and starting to decay by the last snapshot. Similar elongated structures in the same galaxy are seen in the top panel of figure 4. They typically grow and decay on a dynamical timescale.

Figure 10 follows the evolution of an individual gas

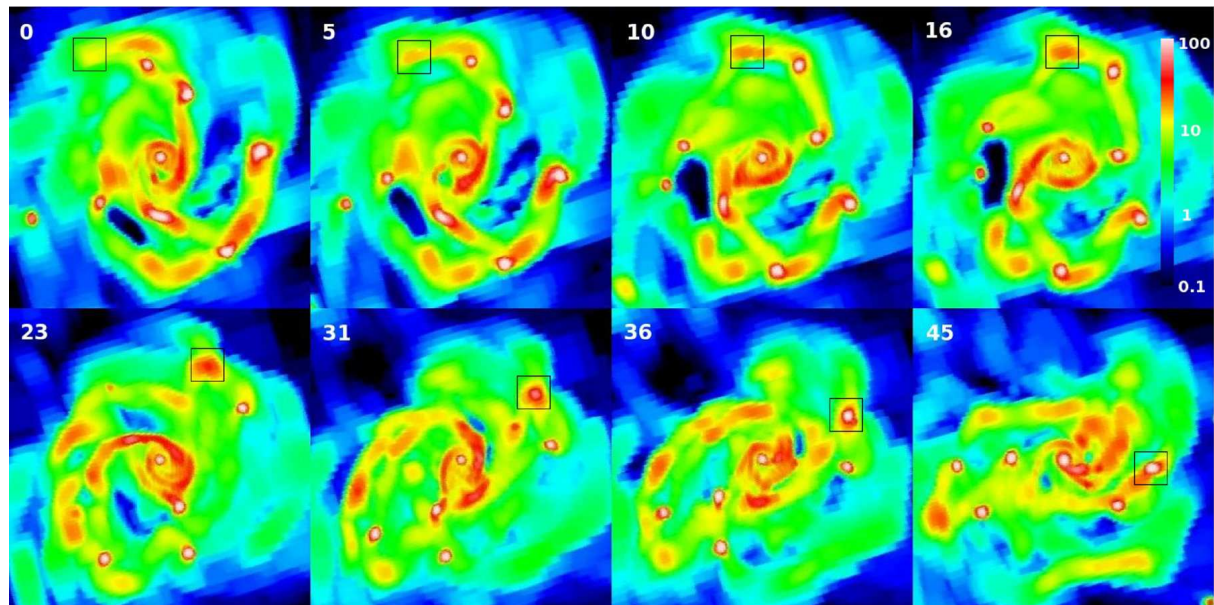


Figure 9. Formation and evolution of a clump. Shown is a time sequence of disc A near $z = 2$. Each snapshot shows the face-on view of the maximum 3D gas density along the line of sight in units of Hydrogen atoms cm^{-3} . The size of each panel is 8 kpc. A black square of size 1 kpc marks the position of one specific clump as it orbits the galaxy. The clump originates as a small-amplitude perturbation in an unstable part of the disc and collapses to virialization within a dynamical time.

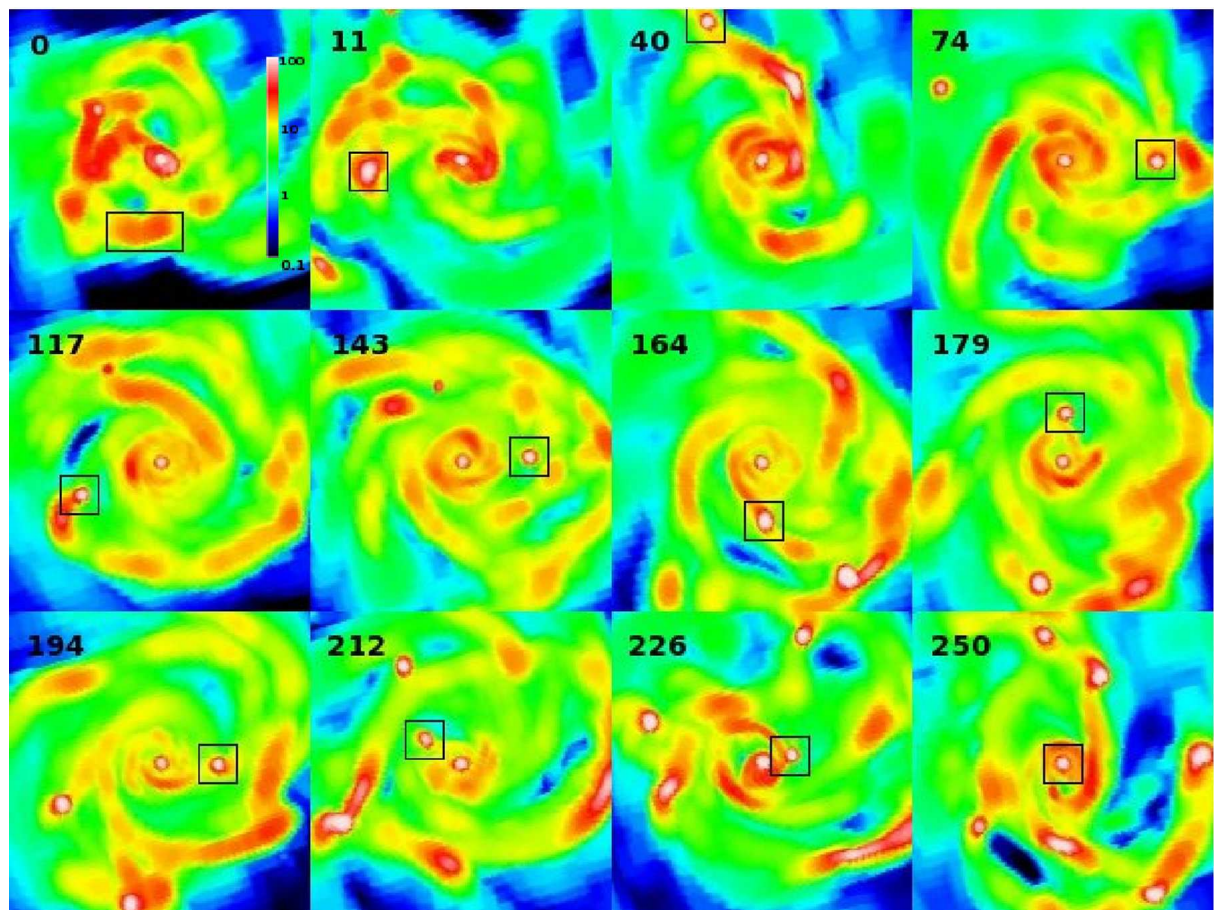


Figure 10. Clump Migration into a bulge. Shown is a time sequence of disc A near $z = 2$. Each snapshot shows the face-on view of the maximum 3D gas density along the line of sight in units of Hydrogen atoms cm^{-3} . The size of each panel is 6 kpc. A black square of size 1 kpc marks the position of one specific clump. The clump forms, virializes, and spirals in. It coalesces with the central bulge in 250 Myr, after completing about four rounds.

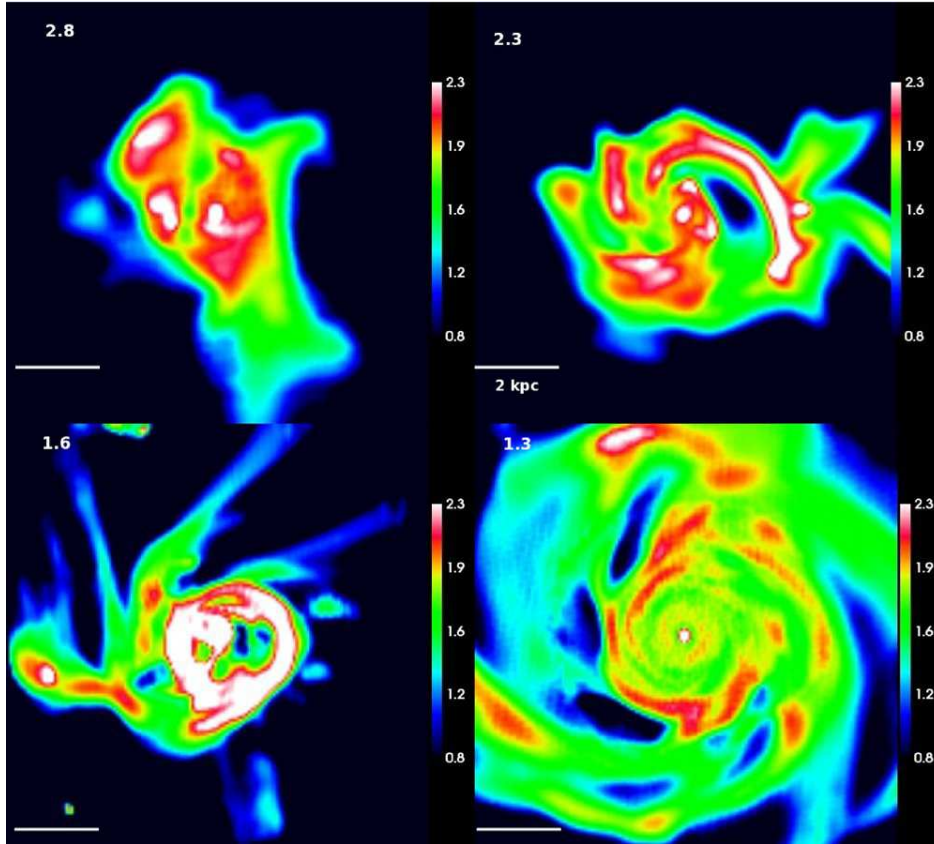


Figure 11. Evolution of galaxy B in steady state over cosmological times. Shown are face-on snapshots of gas surface density at $z = 2.8, 2.3, 1.6, 1.3$ (from left to right) in units of $\log(M_{\odot} \text{pc}^{-2})$. The box side is 10 kpc and the color code is the same in the three panels. This sequence demonstrates that this galaxy maintains a gravitationally unstable disc for at least 2-3 Gyr as it is intensely fed by cosmological cold streams. This steady-state ends near $z = 1.3$, when the disc is stabilized by the presence of a dominant bulge — an example of “morphological quenching”.

clump in galaxy A for a period of 250 Myr, from a pre-collapse cloud to its final coalescence into the bulge. At $t = 0$, we see an elongated broad perturbation. At $t = 40$ Myr, after about one dynamical time, the clump seems collapsed and virialized. As the clump rotates about the galaxy centre it spirals inward, while keeping its size and appearance roughly the same. By $t = 250$ Myr, after circling the centre about four times, the clump has coalesced with the central bulge. The migration time from the outer disc to the centre is $\sim 8t_d$, very similar to the prediction in eq. (6), based on the gravitational interactions within the disc discussed in §2. The SFR inside the clumps starts off at a level of several $M_{\odot} \text{yr}^{-1}$ and it gradually declines as the gas is substantially depleted. While most of the clump mass turns into stars before the migration is over, the clump is still gas rich when it coalesces with the bulge, leading to a compact bulge as in a wet merger.

The migration of clumps to the centre contributes to the growth of the central spheroid. 10-20% of the disc mass flows into the bulge in ten dynamical times, in agreement with the estimated migration time by clump encounters, eq. (6), and the fraction of the disc mass in the clumps, $\alpha \simeq 0.1 - 0.2$. This is equivalent to one or two mergers of mass ratio 1:10 every 0.3 Gyr, which is more than expected on average for standard mergers of satellite clumps that come with the streams from outside the galaxy (Dekel et al. 2009). Thus, the mass inflow in the disc contributes significantly

to the early growth of spheroids. The bulge growth starts as soon as the disc becomes unstable, and it continues for several Gyr in a near steady state, as predicted by DSC. In this steady state, the continuous gas supply is replenishing the draining disc and the comparable bulge and disc keep growing in a similar pace.

5.7 Steady State and Morphological Quenching

Figure 11 shows face-on snapshots of the gas disc of galaxy B from $z = 2.8$ to $z = 1.3$. During most of this period of 2.6 Gyr, the disc appears to be gravitationally unstable, with transient features and bound clumps, similar to its appearance at $z = 2.3$ as analyzed in detail above. This indicates a near steady state, as predicted by DSC. During this period, the gas supplied by the cosmological cold streams replenishes the gas that is being drained into the bulge through clump migration and angular-momentum transport. The value of δ at $z = 2.8, 2.3, 1.6$ is 0.23, 0.27, 0.25 respectively, demonstrating that this steady state is indeed characterized by a roughly even distribution of mass among the disc, bulge and dark matter halo components within the disc radius. A similar steady state is also seen in the other two galaxies. We conclude that the three galaxies simulated here represent the typical stream-fed galaxies observed as rapid star formers at

redshifts 3 to 1.5. A clumpy disc with a smaller bulge could appear within the first 0.5 Gyr after the onset of instability, perhaps following a period of stability due to a dense dark-matter halo, low accretion rate, or high turbulence.

However, one can see in Fig. 11 that by $z = 1.3$, galaxy B is no longer in the steady-state phase. The disc appears to be much smoother than before, showing only minor perturbations of much lower contrast. The disc fraction at this time is only $\delta = 0.2$, indicating that the disc is being stabilized by the presence of a dominant stellar bulge, constituting a significant fraction of the total stellar mass of $M_* \simeq 10^{11} M_\odot$. As a result, the SFR in the disc is reduced to $\sim 5 M_\odot \text{yr}^{-1}$, about a third of the average cosmological accretion rate at this epoch. This is an example of ‘‘morphological quenching’’ of star formation, as discussed and demonstrated in Martig et al. (2009). A similar phenomenon occurs in galaxy A. We note that the buildup of the stabilizing bulge in these galaxies is mostly due to mass inflow in the disc while in the case of Martig et al. (2009) it is predominantly a result of external mergers. This demonstrates that morphological quenching can be obtained in different ways.

We are not in a position to address the properties of the low-redshift descendants of our three simulated galaxies because the simulations were stopped at moderate redshifts, where they became too costly. The last snapshots available for galaxies A and B are at $z = 1.3$, and for galaxy C at $z = 1.9$. The appearance of a dominant stellar spheroid and a minor stable disc of stars and gas in galaxies B and A hints that these galaxies may end up as early-type galaxies with low SFR. On the other hand, as demonstrated by Martig et al. (2009), such galaxies may eventually re-grow a sufficiently massive gas disc that becomes unstable again, and thus turn back into a blue, star-forming, late-type galaxy.

6 ARTIFICIAL FRAGMENTATION

If the Jeans length, λ_J , is comparable to the resolution scale of a grid-based code, i.e., the smallest cell size Δ , one expects artificial fragmentation on that scale. This is because the code fails to properly follow the pressure gradients that are supposed to support a clump on that scale against gravitational collapse. Truelove et al. (1997) have shown that the artificial fragmentation could be prevented if the Jeans length is always resolved by more than 4 resolution elements.¹ If we define a Jeans number by

$$N_J \equiv \frac{\lambda_J}{\Delta}, \quad (9)$$

it has to be kept above a critical value, $N_c = 4$. The Truelove value was obtained based on simulations that lasted only a few free-fall times, so it is possible that a more stringent criterion may be required when the system is followed for longer periods, typical of cosmological simulations.

Our current cosmological simulations do not resolve the thermal Jeans length of the coolest gas, $T \sim 300\text{K}$, so one must act to prevent artificial fragmentation. For this

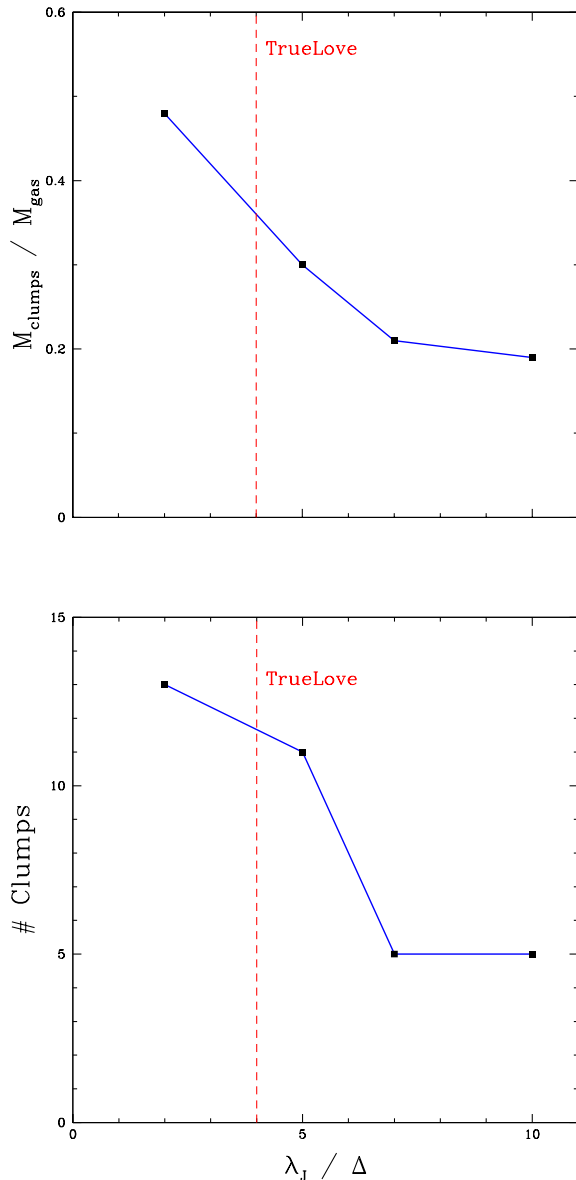


Figure 12. Testing artificial fragmentation. Shown is the mass fraction in clumps (top panel), and the number of clumps (bottom panel) for simulations with different values of N_c . Convergence is indicated at $N_c \geq 7$, and artificial fragmentation becomes gradually more severe as N_c becomes smaller below $N_c = 7$. At the Truelove value, $N_c = 4$, the mass in clumps is larger than the base value at $N_c \geq 7$ by a factor of ~ 1.8 and the number of clumps is higher by a factor of ~ 2.3 . The figure indicates that $N_c \gtrsim 7$ is the recommended value for a pressure floor that would safely eliminate artificial fragmentation.

purpose we have implemented an artificial pressure floor via a procedure that is becoming standard (Machacek et al. 2001; Robertson & Kravtsov 2008; Agertz et al. 2009b). For gas with adiabatic index γ , the speed of sound is related to the pressure and density via $c_s^2 = \gamma P / \rho$, so the Jeans length is given by

$$\lambda_J^2 = \frac{\pi \gamma P}{G \rho^2}. \quad (10)$$

¹ A similar criterion is necessary in SPH simulations, where the Jeans length has to be resolved by more than a given number of SPH kernels (Bate & Burkert 1997).

In order to set the minimum N_J to a desired N_c , we thus set the pressure floor at

$$P_{\text{floor}} = \frac{G\rho^2 N_c^2 \Delta^2}{\pi\gamma}. \quad (11)$$

The pressure in the Euler equation is replaced by an effective pressure that is set to P_{floor} when it would have otherwise obtained a lower value. We adopt $\gamma = 5/3$.

In order to verify the value of N_c necessary for preventing artificial fragmentation in our cosmological discs, we re-ran the simulation of case B for the last 400 Myr prior to $z = 2.3$ with different values of the pressure floor, or N_c . The duration for this test is about 22 dynamical times, which should be sufficient for studying the fragmentation that develops on one or a few dynamical timescales. The corresponding values of N_c were chosen to be 2, 5, 7 and 10, namely from half the Truelove value of $N_c = 4$ to more than twice above it. There is no point testing higher values of N_c because the corresponding Jeans length would have become comparable to the disk thickness and thus prevent the real disk fragmentation that we are after.

Figure 12 shows the fraction of gas in clumps and the number of clumps as a function of N_c . The latter is measured as the number of density peaks with $n > 25 \text{ cm}^{-3}$, and the trend is found to be insensitive to the exact threshold chosen. Below $N_c = 7$, we see a strong increase in both the mass in clumps and the clump number as a function of decreasing N_c . On the other hand, for N_c in the range 7 – 10, we see a convergence of the two clump indicators into constant values. At the Truelove value, $N_c = 4$, both indicators have values about twice as large as their base values at $N_c = 7 - 10$. The similar behavior of the two indicators implies that the artificial fragmentation at small values of N_c is expressed in terms of the appearance of new clumps more than in the growth in mass of the real clumps that exist at large values of N_c .

We conclude that in order to avoid artificial fragmentation, the Jeans length must be resolved by 7 elements or more. We adopt $N_c = 7$ as our default case. With such a pressure floor, the clumps are likely to be real and their global properties are expected to be reliable. They are supported by turbulent motions in the disc and their size is set by the turbulence Jeans length. On the other hand, the detailed internal properties of the clumps, including density profile and substructure, are subject to the limited resolution. This internal structure can be resolved only in simulations of higher resolution.

7 DISCUSSION AND SUMMARY

We analyzed high-resolution AMR simulations of three galaxies in haloes of total mass $\sim 5 \times 10^{11} M_\odot$ and baryonic mass $\sim 5 \times 10^{10} M_\odot$ at $z \simeq 2.3$, selected quite randomly from a cosmological simulation. Each of these cases show a clumpy, thick and turbulent disc of gas and stars extending to (3 – 6) kpc in radius and accommodating a central stellar bulge of comparable mass within the inner (1 – 2) kpc. The discs show a very irregular morphology, with elongated transient features and a few bound massive clumps. The simulations reveal that these are naked clumps, not associated with dark matter haloes, and formed in-situ

in the disc by gravitational instability. The simulated clumpy morphology is remarkably similar to the typical morphology of high-redshift SFGs as observed from different angles of view.

The simulations indeed confirm many of the detailed predictions outlined in Dekel, Sari & Ceverino (2009) based on a straightforward Toomre instability analysis in a cosmological context. They demonstrate that a large fraction of the massive galaxies at $z \simeq 2 - 3$ are made of a gravitationally unstable disc with a stellar bulge of a comparable mass, corresponding to a disc-to-total mass ratio of $\delta \simeq 0.3$ in eq. (4). A significant fraction of the disc has an effective value of $Q \leq 1$, typically defining an extended ring of maximum instability. The in-situ giant clumps are $\sim 10^8 M_\odot$ each, namely on the order of one percent of the disc mass, in agreement with eq. (2). They involve 10-20% of the disc mass, as assumed in DSC. The clumps migrate to the disc centre in about 250 Myr, on the order of ten disc dynamical times, where they coalesce into a bulge. The mass inflow in the disc to the bulge contributes significantly to the spheroid growth, adding to the effect of mergers of external galaxies.

In our simulations, the clumps survive bound until they merge into the bulge. It has been argued that in reality the clumps are disrupted on a dynamical timescale by radiative feedback from newly formed stars (Murray, Quataert & Thompson 2009). In an associated paper (Krumholz & Dekel, in preparation), it is shown that the ejected fraction of gas from the giant clumps in massive disks at high redshift is limited to less than 10% provided that the SFR efficiency is ~ 0.01 , i.e. it obeys the Schmidt-Kennicutt relation between SFR and gas density (Kennicutt 1998), which is also favored theoretically (Krumholz & McKee 2005; Krumholz & Tan 2007). The clumps could be disrupted only if the SFR efficiency was larger than its local value by an order of magnitude.

The SFR at $z = 2.3$ is at the level of $\sim 40 M_\odot \text{ yr}^{-1}$, which is in the ball park of the expected cosmological gas accretion rate along cold streams into haloes of comparable masses (Dekel et al. 2009). This corresponds to more than $100 M_\odot \text{ yr}^{-1}$ in the massive SFGs that reside in haloes more massive than $10^{12} M_\odot$. We recall, though, that the simulated SFR at $z \sim 2.3$ may be slightly underestimated due to the limitations of the sub-grid recipes for star formation and feedback. Given these limitations, about half the star formation seems to occur in the disc clumps. The star formation within each clump extends to $\sim 200 \text{ Myr}$, or several disc dynamical times, which is comparable to the timescale for clump migration. If the star-formation efficiency is $\sim 1 - 2\%$ as in the molecular clouds of today's galaxies (Krumholz et al. 2009), then it must occur in denser sub-clumps (DSC), which are not resolved in our current simulations.

Our simulations confirm that the disc is continuously supplied by fresh material through cold streams that penetrate the hot halo along the dark-matter filaments of the cosmic web. In a companion paper, we use the simulations to predict the observational appearance of these cold streams as extended Lyman-alpha blobs (Goerdt et al. 2009). Despite the very high resolution, the streams in our three galaxies are rather smooth; the fraction of the incoming stream mass in clumps with densities higher than 0.1 cm^{-3} ranges from

7% to 25%, in comparison with the average value of 30% estimated by Dekel et al. (2009) for massive galaxies at similar redshifts. As argued by DSC, this smoothness of the incoming mass is a key for maintaining the disc sufficiently dense and cold without growing a stabilizing bulge, such that the disc is kept gravitationally unstable. The continuous supply of gas keeps this configuration of an unstable disc and a comparable bulge in a near steady state that lasts for 2-3 Gyr.

At least two of the galaxies simulated here become rather stable before $z = 1$; they become dominated by a stellar spheroid that stabilizes the remaining disc, prevents its fragmentation into giant clumps, and suppresses star formation to quiescent levels. This is a demonstration of the morphological-quenching mechanism discussed by Martig et al. (2009) and seen in the simulation of Agertz et al. (2009b).

Two of the simulated galaxies show a mass fraction of galactic baryons inside the dark-matter halo which is $\sim 30\%$ of the cosmological baryonic fraction, while the third galaxy has a baryon fraction comparable to the universal value. The comparison with the low baryonic fractions indicated from observations at low redshift (e.g., F. Prada, private communication) is beyond the scope of this paper, because our simulations are currently limited to high redshift. We anticipate that low baryonic fractions can be obtained if the baryon accretion is suppressed at low redshifts while the dark-matter haloes keep growing.

While the current simulations are state of the art, they are still limited in many ways. One limiting issue is the relatively low gas fractions of 8 – 35% in the simulated discs compared to the values of 30 – 60% indicated for the observed galaxies. Although the observational estimates are indirect and therefore uncertain, it is possible that our current simulations slightly overestimate the star formation rate at earlier times, possibly as a result of underestimating the suppression of SFR by stellar and supernova feedback. This may lead to an underestimate of the gas fraction and SFR at $z = 2.3$. Fortunately, this possible limitation does not prevent the robust appearance of strong instability in the high-redshift discs at $z \geq 1.5$, so the simulations do produce galaxies that mimic the main features of the observed SFGs and the theoretical predictions.

Another caveat is associated with the mandatory incorporation of a pressure floor. While it serves the purpose of preventing artificial fragmentation, it necessarily smoothes the thermal-pressure gradients in high density regions. Only simulations with a resolution better than 10 pc could help us directly evaluate the side effects that may be introduced by this pressure floor on small scales. However, the tests presented in §6 demonstrate that the global properties of the clumps are stable against variations of the pressure floor in the regime where artificial fragmentation is suppressed. This is because the gravitational collapse of the clumps is balanced by velocity dispersion rather than by thermal pressure gradients. The velocity associated with the artificial pressure is $\sim 8 \text{ km s}^{-1}$ compared to the turbulent velocity of 20 – 30 km s^{-1} . In practice, over most of the simulated unstable disks, the Jeans length associated with the overall pressure is significantly larger than the artificial minimum imposed at 7 cell sizes.

Our main findings from the clumpy galaxies at

high redshift are consistent with the parallel findings of Agertz et al. (2009b), who used a simulation with a similar resolution but a different AMR code. They also see clump formation in massive spiral arms driven by disc instability. However, they find about twice as many bound clumps, ranging to smaller masses and preferentially populating the outer disc, which seem not to resemble the observed SFGs as well as our simulations. Furthermore, they detect significant small-scale fragmentation in the initially smooth, cold streams, where we see no such effect. This is probably a result of some degree of artificial fragmentation in Agertz et al. (2009b) due to the lower pressure floor adopted in their simulation, (§6). When resolving the Jeans length with only 4 resolution elements, following the Truelove criterion, we find that artificial fragmentation tends to occur in regions where the gas velocity dispersion is low such that the Jeans length is strongly affected by thermal pressure, as in the coherent cold streams. On the other hand, when we resolve the Jeans length by 7 resolution elements, we prevent such artificial fragmentation in our simulations. Still, the many qualitative similarities between the findings of Agertz et al. (2009b) and ours indicate that we both capture the real key features of high-redshift SFGs.

We conclude that zoom-in simulations of galaxies drawn quite randomly from a cosmological volume reproduce clumpy discs and bulges similar to the observed star-forming galaxies at high redshift. The simulations demonstrate the validity of the simple theoretical picture where the continuous gas supply by cold streams drives a self-regulated gravitational instability in a cosmological steady state that tends to last for several Gyr.

ACKNOWLEDGMENTS

The computer simulations were performed at the National Energy Research Scientific Computing Center (NERSC), Lawrence Berkeley National Laboratory, PI J. Primack. We acknowledge stimulating discussions with Andi Burkert, Bruce Elmegreen, Reinhard Genzel, Tobias Goerdt, Anatoly Klypin, Mark Krumholz, Doug Lin, Joel Primack, Re'em Sari, Kristen Shapiro, Amiel Sternberg and Linda Tacconi. This research has been partly supported by an ISF grant, by GIF I-895-207.7/2005, by a DIP grant, by a France-Israel Teamwork in Sciences, by the Einstein Center at HU, and by NASA ATP NAG5-8218 at UCSC. DC is a Golda-Meir Fellow at HU.

REFERENCES

- Adelberger, K. L., Steidel, C. C., Shapley, A. E., Hunt, M. P., Erb, D. K., Reddy, N. A., & Pettini, M. 2004, *ApJ*, 607, 226
- Agertz, O., Lake, G., Teyssier, R., Moore, B., Mayer, L., & Romeo, A. B. 2009, *MNRAS*, 392, 294
- Agertz, O., Teyssier, R., & Moore, B. 2009, *MNRAS*, 397, L64
- Bate, M. R., & Burkert, A. 1997, *MNRAS*, 288, 1060
- Bezanson, R., van Dokkum, P. G., Tal, T., Marchesini, D., Kriek, M., Franx, M., & Coppi, P. 2009, arXiv:0903.2044
- Binney, J. 2004, *MNRAS*, 347, 1093

- Binney J., Tremaine S., 2008, *Galactic Dynamics*. Princeton Univ. Press, Princeton, NJ
- Birnboim, Y., & Dekel, A. 2003, *MNRAS*, 345, 349
- Birnboim, Y., Dekel, A., & Neistein, E. 2007, *MNRAS*, 380, 339
- Bolatto, A. D., Leroy, A. K., Rosolowsky, E., Walter, F., & Blitz, L. 2008, *ApJ*, 686, 948
- Bouché, N., et al. 2007, *ApJ*, 671, 303
- Bournaud, F., Elmegreen, B. G., & Elmegreen, D. M. 2007, *ApJ*, 670, 237
- Bournaud, F., et al. 2008, *A&A*, 486, 741
- Bournaud, F., & Elmegreen, B. G. 2009, *ApJ*, 694, L158
- Bournaud, F., et al., 2009, submitted
- Bruzual, G., & Charlot, S. 2003, *MNRAS*, 344, 1000
- Cattaneo, A., Dekel, A., Devriendt, J., Guiderdoni, B., & Blaizot, J. 2006, *MNRAS*, 370, 1651
- Ceverino, D., & Klypin, A. 2009, *ApJ*, 695, 292
- Cowie, L. L., Hu, E. M., & Songaila, A. 1995, *AJ*, 110, 1576
- Cox, T. J., Dutta, S. N., Di Matteo, T., Hernquist, L., Hopkins, P. F., Robertson, B., & Springel, V. 2006, *ApJ*, 650, 791
- Cresci, G., et al. 2009, *ApJ*, 697, 11
- Daddi, E., Cimatti, A., Renzini, A., Fontana, A., Mignoli, M., Pozzetti, L., Tozzi, P., & Zamorani, G. 2004, *ApJ*, 617, 746
- Daddi, E., Dannerbauer, H., Elbaz, D., Dickinson, M., Morrison, G., Stern, D., & Ravindranath, S. 2008, *ApJ*, 673, L21
- Daddi, E., et al. 2009, arXiv:0911.2776
- Dekel, A., & Silk, J. 1986, *ApJ*, 303, 39
- Dekel, A., & Birnboim, Y. 2006, *MNRAS*, 368, 2
- Dekel, A., & Cox, T. J. 2006, *MNRAS*, 370, 1445
- Dekel, A., et al. 2009, *Nature*, 457, 451
- Dekel, A., Sari, R., & Ceverino, D. 2009, *ApJ*, 703, 785 (DSC)
- Elmegreen, D. M., Elmegreen, B. G., & Sheets, C. M. 2004, *ApJ*, 603, 74
- Elmegreen, D. M., Elmegreen, B. G., & Hirst, A. C. 2004, *ApJ*, 604, L21
- Elmegreen, B. G., & Elmegreen, D. M. 2005, *ApJ*, 627, 632
- Elmegreen, D. M., Elmegreen, B. G., Rubin, D. S., & Schaffer, M. A. 2005, *ApJ*, 631, 85
- Elmegreen, B. G., & Elmegreen, D. M. 2006, *ApJ*, 650, 644
- Elmegreen, D. M., Elmegreen, B. G., Ravindranath, S., & Coe, D. A. 2007, *ApJ*, 658, 763
- Elmegreen, B. G., Elmegreen, D. M., Ximena Fernandez, M., & Lemonias, J. J. 2008c, *ApJ*, 691, 23
- Elmegreen, B. G., Bournaud, F., & Elmegreen, D. M. 2008, *ApJ*, 688, 67
- Elmegreen, B. G., Elmegreen, D. M., Fernandez, M. X., & Lemonias, J. J. 2009, *ApJ*, 692, 12
- Elmegreen, D. M., Elmegreen, B. G., Marcus, M. T., Shahinyan, K., Yau, A., & Petersen, M. 2009, arXiv:0906.2660
- Erb, D. K., Steidel, C. C., Shapley, A. E., Pettini, M., Reddy, N. A., & Adelberger, K. L. 2006, *ApJ*, 646, 107
- Förster Schreiber, N. M., et al. 2006, *ApJ*, 645, 1062
- Förster Schreiber, N. M., et al. 2009, *ApJ*, 706, 1364
- Genel, S., Genzel, R., Bouché, N., Naab, T., & Sternberg, A. 2008, arXiv:0812.3154
- Genzel, R., et al. 2006, *Nature*, 442, 786
- Genzel, R., et al. 2008, *ApJ*, 687, 59
- Goldreich, P., & Lynden-Bell, D. 1965, *MNRAS*, 130, 97
- Goerdt, T., Dekel, A., Sternberg, A., Ceverino, D., Teyssier, R., & Primack, J. R. 2009, arXiv:0911.5566
- Governato, F., Willman, B., Mayer, L., Brooks, A., Stinson, G., Valenzuela, O., Wadsley, J., & Quinn, T. 2007, *MNRAS*, 374, 1479
- Greve, T. R., et al. 2005, *MNRAS*, 359, 1165
- Heyer, M., Krawczyk, C., Duval, J., & Jackson, J. M. 2008, arXiv:0809.1397
- Hopkins, P. F., Hernquist, L., Cox, T. J., Di Matteo, T., Robertson, B., & Springel, V. 2006, *ApJS*, 163, 1
- Immeli, A., Samland, M., Gerhard, O., & Westera, P. 2004, *A&A*, 413, 547
- Immeli, A., Samland, M., Westera, P., & Gerhard, O. 2004, *ApJ*, 611, 20
- Jog, C. J., & Solomon, P. M. 1984, *ApJ*, 276, 127
- Kennicutt, R. C., Jr. 1998, *ApJ*, 498, 541
- Kereš, D., Katz, N., Weinberg, D. H., & Davé, R. 2005, *MNRAS*, 363, 2
- Komatsu, E., et al. 2009, *ApJS*, 180, 330
- Klypin, A., Kravtsov, A. V., Bullock, J. S., & Primack, J. R. 2001, *ApJ*, 554, 903
- Kravtsov, A. V., Klypin, A. A., & Khokhlov, A. M. 1997, *ApJS*, 111, 73
- Kravtsov, A. V. 2003, *ApJ*, 590, L1
- Kriek, M. et al. 2006, *ApJ*, 649, L71
- Kriek, M., van Dokkum, P. G., Franx, M., Illingworth, G. D., & Magee, D. K. 2009, *ApJ*, 705, L71
- Krumholz, M. R., & McKee, C. F. 2005, *ApJ*, 630, 250
- Krumholz, M. R., & Tan, J. C. 2007, *ApJ*, 654, 304
- Krumholz, M. R., McKee, C. F., & Tumlinson, J. 2009, *ApJ*, 699, 850
- Law, D. R., Steidel, C. C., Erb, D. K., Larkin, J. E., Pettini, M., Shapley, A. E., & Wright, S. A. 2007, *ApJ*, 669, 929
- Law, D. R., Steidel, C. C., Erb, D. K., Larkin, J. E., Pettini, M., Shapley, A. E., & Wright, S. A. 2009, arXiv:0901.2930
- Machacek, M. E., Bryan, G. L., & Abel, T. 2001, *ApJ*, 548, 509
- Martig, M., Bournaud, F., Teyssier, R., & Dekel, A. 2009, arXiv:0905.4669
- McKee, C. F., & Ostriker, E. C. 2007, *ARA&A*, 45, 565
- Murray, N., Quataert, E., & Thompson, T. A. 2009, arXiv:0906.5358
- Neistein, E., van den Bosch, F. C., & Dekel, A. 2006, *MNRAS*, 372, 933
- Noguchi, M. 1999, *ApJ*, 514, 77
- Ocvirk, P., Pichon, C., & Teyssier, R. 2008, *MNRAS*, 390, 1326
- Prochaska, J. X. 1999, *ApJ*, 511, L71
- Rafikov, R. R. 2001, *MNRAS*, 323, 445
- Robertson, B., Yoshida, N., Springel, V., & Hernquist, L. 2004, *ApJ*, 606, 32
- Robertson, B., Cox, T. J., Hernquist, L., Franx, M., Hopkins, P. F., Martini, P., & Springel, V. 2006, *ApJ*, 641, 21
- Robertson, B. E., & Kravtsov, A. V. 2008, *ApJ*, 680, 1083
- Robertson, B. E., & Bullock, J. S. 2008, *ApJ*, 685, L27
- Shapiro, K. L., et al. 2008, *ApJ*, 682, 231
- Springel, V., & Hernquist, L. 2003, *MNRAS*, 339, 289
- Stark, D. P., Swinbank, A. M., Ellis, R. S., Dye, S., Smail,

- I. R., & Richard, J. 2008, *Nature*, 455, 775
- Steidel, C. C., Adelberger, K. L., Giavalisco, M., Dickinson, M., & Pettini, M. 1999, *ApJ*, 519, 1
- Stewart, K. R., Bullock, J. S., Barton, E. J., & Wechsler, R. H. 2009, *ApJ*, 702, 1005
- Tacconi, L. J., et al. 2006, *ApJ*, 640, 228
- Tacconi, L. J., et al. 2008, *ApJ*, 680, 246
- Toomre, A. 1964, *ApJ*, 139, 1217
- Truelove, J. K., Klein, R. I., McKee, C. F., Holliman, J. H., II, Howell, L. H., & Greenough, J. A. 1997, *ApJ*, 489, L179
- van den Bergh, S., Abraham, R. G., Ellis, R. S., Tanvir, N. R., Santiago, B. X., & Glazebrook, K. G. 1996, *AJ*, 112, 359
- van Dokkum, P. G. et al. 2008, *ApJ*, 677, L5
- Wolfe, A. M., Gawiser, E., & Prochaska, J. X. 2005, *ARA&A*, 43, 861

This paper has been typeset from a $\text{\TeX}/\text{\LaTeX}$ file prepared by the author.